PERIODICO di MINERALOGIA
established in 1930

DIPARTIMENTO
DI SCIENZE DELLA TERRA

SAPIENZA
UNIVERSITÀ DI ROMA

An International Journal of
Mineralogy, Crystallography, Geochemistry,
Ore Deposits, Petrology, Volcanology
and applied topics on Environment, Archaeometry and Cultural Heritage

Origin of Lower Paleozoic S-type magmatism in a northern terrane of Gondwana (Central Iran): Geochemical and isotopic approach

Nargess Shirdashtzadeh [1], Ghodrat Torabi [1,*], Thomas C. Meisel [1], Chris Harris [3], Tomoaki Morishita [4,5], Akihiro Tamura [5]

[1] Department of Geology, University of Isfahan, P.O. Box: 8174673441, Isfahan, Iran
[2] General and Analytical Chemistry, Montanuniversität, 8700 Leoben, Austria
[3] Department of Geological Sciences, University of Cape Town, Rondebosch 7701, South Africa
[4] Lamont-Doherty Earth Observatory, Columbia University, Palisades, New York 10964, U.S.A.
[5] School of Natural System, College of Science and Engineering, Kanazawa University, 920-1192 Kanazawa, Japan

ARTICLE INFO

Submitted: February 2020
Accepted: April 2020
Available on line: April 2020

* Corresponding author:
torabighodrat@sci.ui.ac.ir

DOI: 10.2451/2020PM16608

How to cite this article:
Shirdashtzadeh N. et al. (2020)
Period. Mineral. 89, 189-213

ABSTRACT

In the center of Iran, Central-East Iranian Microcontinent (CEIM) was a part of Gondwana supercontinent in pre-Palaeozoic during Pan-African Orogeny. It is a zone of several tectonomagmatic and metamorphic episodes from Neoproterozoic to earliest Palaeozoic. In the north of CEIM, Airekan granite is a relic of Paleozoic magmatism in northern Gondwana. It is potentially a significance pluton that preserved the magmatic/metamorphic evolution of the active continental margin of the vanished Ocean of Proto-Tethys. This pluton is characterized by SiO_2>70 wt%, A/CNK>1, Rb>~160 ppm, Y<50 ppm, Th<30 ppm, Th/Ta>5. The $\delta^{18}O$ value of quartz (average ~11.86 ‰; n=8), calculated $\delta^{18}O$ value of whole rock (average ~10.75 ‰), absence of hornblende, presence of biotite, muscovite and inherited zircon, high content of orthoclase, and microgranular granitic enclaves are all consistent with it being a continental collision-related peraluminous S-type granite. Th+U versus $^{206}Pb/^{238}U$ ratios of zircons correlate with decreasing crystallization temperatures related to the Cambrian-Ordovician magmatic events preserved in the inherited and magmatic zircons, toward their Devonian metamorphic overgrowth occurred via Caledonian Orogeny. The Airekan granite probably formed by mica-dehydration melting at ~690-820 °C/10-15 kbar, and it is geochronologically and geochemically comparable with other Gondwanan collision-related granitic plutons (along north of Africa, Turkey, Iran to Himalaya).

Keywords: Gondwana; Iran; granite; geochemistry; oxygen isotope.

INTRODUCTION

Several subduction-related magmatisms have occurred along the northern margin of the Gondwana Supercontinent in the middle-east (e.g., Ramezani and Tucker, 2003; Rossetti et al., 2015; Shafaii Moghadam et al., 2016; Badr et al., 2018, etc.). Iran is currently one of the main segments of the Alpine-Himalayan orogenic system with a complex Permian to Quaternary history of successive rifting and collision (e.g. Verdel et al., 2007). It has preserved several tectonic, magmatic, and metamorphic imprints from Neoproterozoic to earliest Palaeozoic evolution when it was a part of Gondwana supercontinent in pre-Palaeozoic during Pan-African Orogeny (equivalent with Cadomian Orogeny). Several

dispersed Cadomian basement rocks are also found in Central Iran, the Sanandaj-Sirjan Zone and the Alborz Mountains, as well as in the Tauride-Anatolide platform in western Anatolia and in NW Turkey interpreted to show fragments of Neoproterozoic-early Cambrian continental arcs bordering the northern active margin of Gondwana (Shafaii Moghadam et al., 2016). In the middle of Iran, Central-East Iranian Microcontinent (=CEIM) (Figure 1) was an area of continuous magmatisms and deformations, in response to Neoproterozoic to Cenozoic ongoing convergence between the Arabian (Gondwana) and Eurasian plates (e.g., Nadimi, 2007). In CEIM, several well-known Palaeozoic to Mesozoic granitoid plutons have occurred (Figure 1a), including: Narigan (Mosavi Makoi, 1998), Chador-Malu (Ramezani and Tucker, 2003), Zarigan (Ramezani and Tucker, 2003), Airekan, Esmael-Abad (Ramezani and Tucker, 2003), and Shirkuh (Sheibi et al., 2012).

The granites are the most abundant plutonic rocks that can represent probes into the evolution of continental crust and subduction zones. Origin and classification of granites were the main theme of many researches (e.g., Chappell and White, 1974; Barbarin, 1999; Frost et al., 2001, etc.). One of the most commonly used classification schemes for granites was suggested by Chappell and White (1974), in which granites are defined as I-, S-, A-

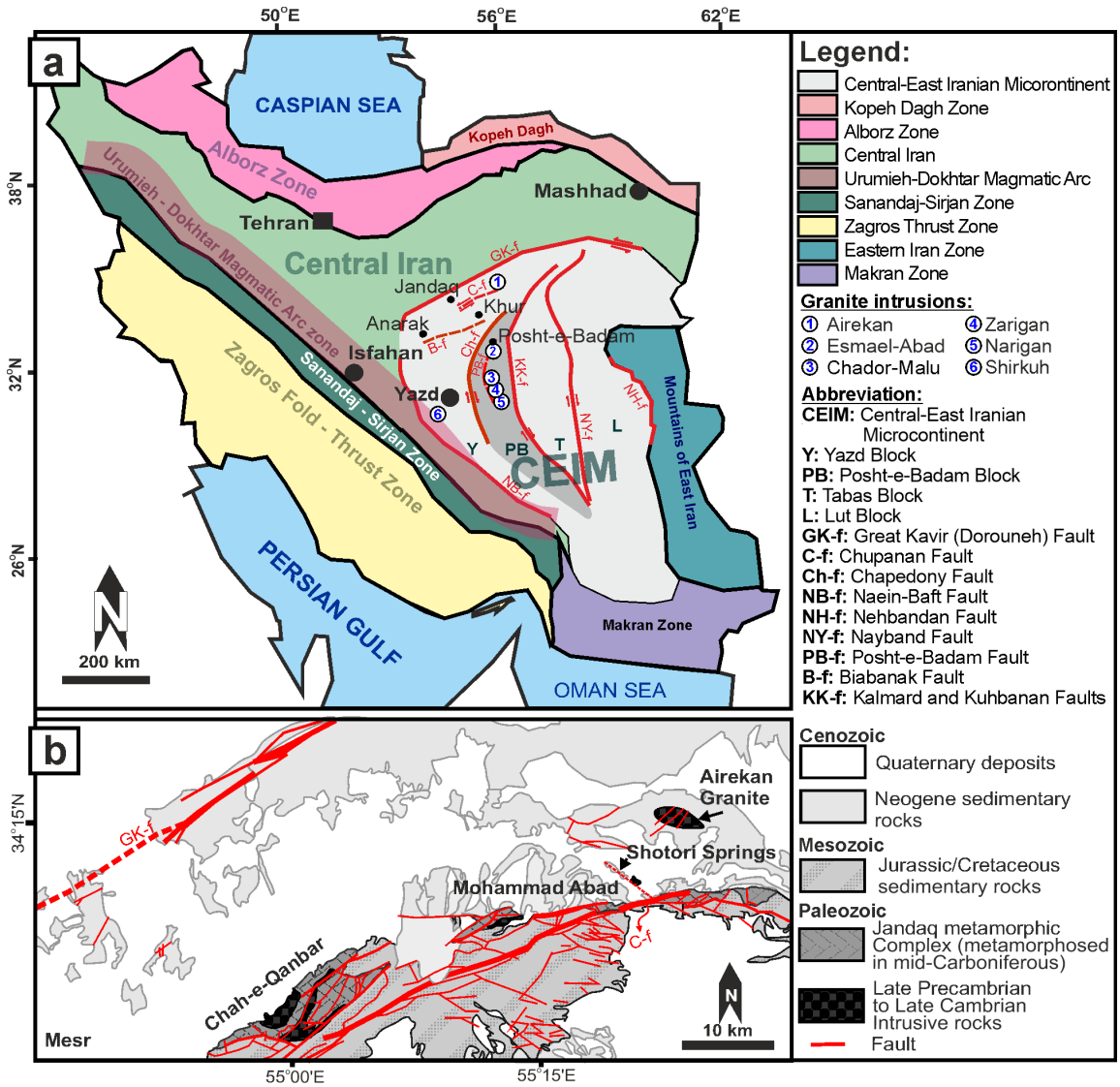

Figure 1. (a) Simplified map of structural and lithological domains in Iran and Central-East Iranian Microcontinent (CEIM) in details. Numbered circles show the location of some granitic intrusions in Yazd and Posht-e-Badam Blocks; (b) Geological map of Airekan area in the north of Khur (Yazd Block, CEIM), based on 1:100000 scale map of Arusan (sheet 7058) by Susov et al. (1984).

and M- types. A key factor in S-type granite generation is to have a metasedimentary source buried in the deep crust before anatexis in a collisional system (e.g., Barbarin, 1999, and references therein), however, most S-type granites may form under thickening of a preexisting, sediment-dominated backarc basin (Collins and Richards, 2008).

The Airekan granite is one of the key plutons of Gondwana exposed within the Miocene Upper Red Formation in the western segment of the Yazd Block in CEIM (Figure 1a). Petrological studies on this granite provide insights to the tectonomagmatic evolution of CEIM in late Cambrian - early Ordovician. However, limited petrological and geochemical studies have performed on this pluton due to difficult access. This study is the first detailed geochemical research performed on the petrology of the Airekan pluton. By using various precise geochemical methods (Oxygen isotope, EPMA and LA-ICP-MS analysis of minerals and ICP-MS analysis of whole rock samples), this study sheds some light on the Cambrian- Ordovician magmatic evolution in northern Gondwana terranes.

GEOLOGICAL BACKGROUND

Gondwana existed at the time of formation of Pangaea, and it remained intact after breaking up the Pangaea. It was first assembled by continental collisions from Late Precambrian to Cambrian (about 800 to 550 Ma) (e.g., Meert and Van Der Voo, 1997, etc.) during Pan-African Orogeny. By Early Ordovician, the Ediacaran-Carboniferous ocean of Proto-Tethys (an ocean between Proto-Laurasia in the north and Proto-Gondwana in the south) was closed and subducted under different segments of the Gondwana margin from Greece, Turkey and Iran to Himalaya (e.g., von Raumer and Stampfli, 2008; Rossetti et al., 2015; Shafaii Moghadam et al., 2016). Therefore, the supercontinent of Proto-Pangea (e.g., Li et al., 2017), formed by several subduction-related magmatic events at the northern margin of the Gondwana. Then, Middle Cambrian-Late Triassic ocean of Paleo-Tethys occurred along the northern margin of Gondwana during Caledonian to Hercynian Orogeny. During the early Permian - Triassic, Paleo-Tethys Ocean subducted, Neo-Tethys Ocean opened, and consequently, Cimmerian terranes including several parts of Iran (i.e., NW Iran, Alborz, Central Iran, and Sanandaj-Sirjan) moved toward Eurasia (e.g. Muttoni et al., 2009). Meantime, the breakup of Gondwana occurred in several stages from Early Jurassic Period, about 180 million years ago, Lower Cretaceous, and during the Upper Cretaceous Period. Then, mountain building occurred along the closure of Tethyan Ocean from Balkans through southern Turkey, northern Iraq, Iran, and Afghanistan, eventually reaching the Himalayas, during Alpine-Himalayan orogeny from Triassic to Late Oligocene-Miocene and later to form the present-day geomorphology of Iran.

Central - East Iranian Microcontinent

Iran is a part of terranes from the west of Gondwana, migrated toward Eurasia in early Permian - Triassic by Cimmerian orogeny and affected by several collisional tectonic during Alpine-Himalayan orogenic system from Triassic to now. Complex tectonic, magmatic and metamorphic evolution resulted in occurrence of different geological and structural units of Iran (from SW to E), including the Zagros thrust zone (ZTZ), Sanandaj-Sirjan metamorphic zone (SSZ), Urumieh-Dokhtar magmatic arc (UDMA), Central-East Iranian Microcontinent (CEIM), Alborz, Kopeh Dagh, Eastern Iran, and Makran zones (Figure 1a).

The Central - East Iranian Microcontinent is between Arabian and Eurasian Plates and surrounded by faults and the remnants of several Tethyan Oceanic crusts (e.g., Naein, Ashin, Iranshahr, Fanuj-Maskutan, Band-e-Ziarat, Esfandagheh, Baft, and Surk ophiolites; Shirdashtzadeh et al., 2014, etc.). It comprises four major Pan-African (early Cambrian) crustal domains with individual deformation style and seismicity, including blocks of Lut, Tabas (Kerman-Tabas), Posht-e-Badam, and Yazd (Naein), separated by a series of intersecting faults with nearly north to south direction (e.g., Alavi, 1991) (Figure 1a). Most of the granitoid intrusions (i.e., Zarigan, Narigan. Chador-Malu, Shirkuh, Esmael-Abad, and Airekan) in CEIM are exposed in its western segments (i.e., Yazd and Posht-e-Badam blocks; Figure 1a). The Yazd Block is located between the Chupanan Fault to the east, the Great Kavir Fault to the north and the Naein-Baft Fault to the south and west (Figure 1a). In Yazd block, the NE-SW oriented, left-lateral active fault of Chupanan has separated the late Precambrian rocks (i.e., Chah-e-Qanbar granite; Bagheri and Stampfli, 2008) in the north from the mid-Carboniferous metamorphic rocks of Anarak-Jandaq terrane in the south (Figure 1b).

Airekan granite in the Yazd Block

The study area of Airekan is a region in the north of Khur in the northern part of Yazd Block (Figure 1a). Airekan intrusion is an elliptical dark colored mountainous massif along with northwest - southeast. It has a peak elevation of ~935 m and 5.6 km^2 in area and several fault and fractures have crosscut the outcrop in NE-SW direction (Figure 2a). It is exposed within Neogene sediments of Upper Red Formation (Figure 2b).

The early age determinations for Airekan pluton by Reyre and Mohafez (1972) include Rb-Sr dates of whole rock samples (165±8 Ma; Calloyian, Middle Jurassic)

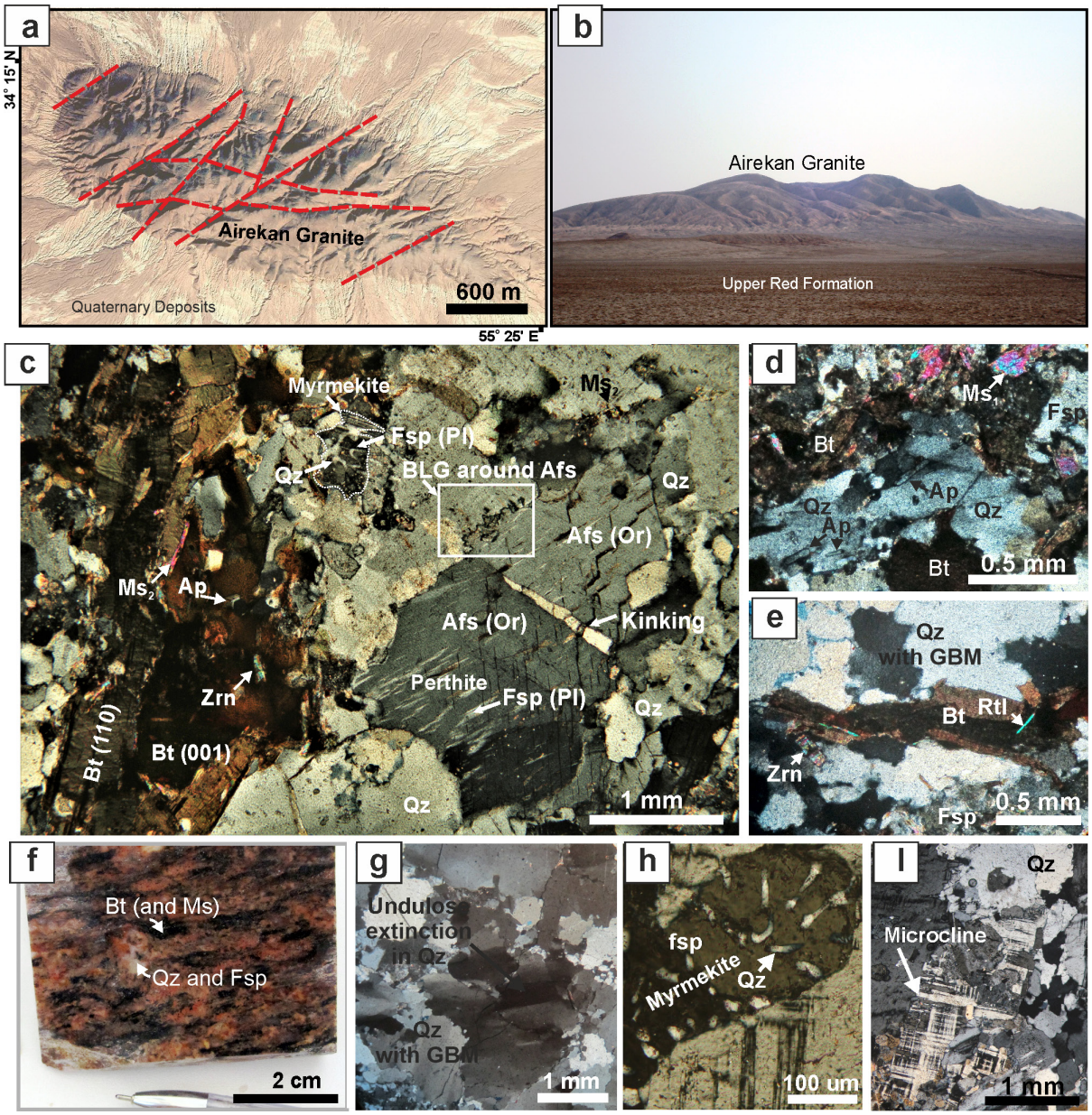

Figure 2. (a) A closer view of Airekan granite (north of Yazd Block, CEIM) and its fault system in a sheared zone; (b) Field view of Airekan pluton within Cenozoic Upper Red Formation deposit; (c-e) Photomicrographs (in plane polarized light) for deformed igneous textures and mineralogy, including quartz with GBM recrystallization, deformed alkali-feldspar (orthoclase) with BLG recrystallization, kinking, formation of flame perthite and myrmekite, biotite with zircon inclusions, primary muscovite and tiny crystal of secondary muscovite (occurred between quartz and feldspar and at the expense of biotite alteration), inherited zircon with pleochroic halo, apatite and rutile; (f) hand specimen of a foliated granite with alternating layers of felsic and mafic minerals; (g) GBM and undulose extinction in quartz grains; (h) Myrmekite formed during deformation; (i) Microcline formed during deformation (Abbreviations of mineral names are from Whitney and Evans (2010)).

and K-Ar dating of minerals (113±9 Ma for biotite and 74±13 Ma for K-feldspar samples). In previous works, Airekan were known to be similar to the granite gneiss of Chah-e-Qanbar (e.g., Romanko et al., 1979; Bagheri and Stampfli, 2008) and Mohammad Abad (Figure 1b) and as a part of a single batholith exposed along tectonic uplifts. However, the recent U-Pb dating of zircons indicated that granitic gneiss in Chah-e-Qanbar (549±15 Ma; including 3 zircon grains in sample Ja04-1-9 from Chah-e-Qanbar; Bagheri and Stampfli, 2008) are older

than the U-Pb age of Airekan granite (Shirdashtzadeh, 2017; Shirdashtzadeh et al., 2018). The most recent and complete U-Pb dating of zircons (including 29 zircon grains) in Airekan by Shirdashtzadeh et al. (2018) has yielded: (1) Neoproterozoic to Cambrian (~518.2±4.9 Ma for 5 distinctive inherited zircons and zircons, but zircons with 554, 614, 679 and 892 Ma ages are also found) for an ancient magmatic stage; (2) late Cambrian to early Ordovician (483±2.9 Ma) for a younger magmatic stage; (3) Devonian age (~382.6±3.2 Ma) for partial resetting of the U-Pb isotope system in zircons during high- grade solid-state deformation and/or metamorphism.

ANALYTICAL METHODS

Twenty-five rock samples with the least alteration were selected from different parts of the pluton (fourteen from granite, ten from aplitic dikes, and two from enclaves). Six thin sections of granite, aplitic dike, and enclave are selected and carbon coated for EPMA analysis of minerals. Spots suitable for further analysis by EPMA or LA-ICPMS were selected as free of inclusions and/or cracks, with perpendicular grain edges (no underlying wedges), and with an immaculate surface polish.

Quantitative chemical analyses of minerals including quartz, feldspars, and micas (Table 1) were carried out using a JEOL JXA8800R wavelength-dispersive electron probe micro-analyzer (EPMA) at Kanazawa University (Kanazawa, Japan), equipped with five wavelength-dispersive spectrometers with various LIF, PET and TAP crystals. The analyses were performed with an accelerating voltage of 15 kV and a beam current of 15 nA (on Faraday cup), using a 3 μm beam diameter. Natural and synthetic minerals of known composition were used as standard. All elements were measured by WDS on their K-lines, collecting 10-30 s on both peak and background. Raw element data were corrected using the ZAF corrections of JEOL software. The method largely follows that of Morishita et al. (2018).

The REE and other trace-element (Rb, Sr, Y, Ba, Ta, Pb, Th, U) compositions of selected minerals (Table 2) were determined by laser ablation-inductively coupled plasma mass spectrometry (LA-ICP-MS) using a 193 nm ArF Excimer Laser coupled to an Agilent 7500S at the Earth Science Department of the Kanazawa University (Japan). The diameter of the analyzed points was 60 micrometers to optimize sensitivity at a frequency of 8 Hz. Details of the analytical methods and data quality were described by Morishita et al. (2018).

For the determination of major and trace element mass fractions of whole rock samples (Table 3), a combination of lithium tetraborate used beads X-ray fluorescence (WXRF, Axios Panalytical/Malvern) analysis and sodium peroxide sintering with ICP-MS (Agilent 7500; Chair General and Analytical Chemistry at the Montanuniverisät Leoben in Austria). The external calibration of the XRF and the ICP-MS was established using certified and non-certified geological reference materials from the USGS and IAG mainly. In order to complete digestion of samples with refractory minerals (e.g., zircon), the methods by Meisel et al. (2002) and Bokhari and Meisel (2017) are used. In brief, 100 mg sample powder was mixed with 600 mg finely ground Na_2O_2, sintered at about 480 °C, and dissolved in 3 mol/l HCl.

Representative zircon crystals were extracted from the granite samples by hand-picking under a binocular microscope and mounted in resin and polished. The internal structures of the zircons were assessed visually by cathodoluminescence (CL), using a Zeiss EVO SEM with a Tungsten source at Macquarie GeoAnalytical (Macquarie University, Australia). Then A New Wave UP-213 laser ablation system (5 Hz repetition rate, 30 μm spot size) with a cell affording a <10s total washout and an attached Agilent 7700 Series ICP-MS was used to ablate the representative zircon grains. Details of the analytical method and data quality are available in Shirdashtzadeh et al. (2018). The acquired data on the isotope ratios are presented in Table 4.

For oxygen isotope measurements, quartz grains are separated from eight granite and three aplitic dike samples. All O-isotope data were obtained at the University of Cape Town. About 3 mg of cleaned and hand-picked quartz grains were analyzed by the laser fluorination method described by Harris and Vogeli (2010). Each sample was reacted in the presence of approximately 10 kPa BrF5. The purified O_2 was then collected on a 5 Å molecular sieve in a glass storage bottle. All isotope ratios (Table 5) were measured using a Finnigan Delta XP mass spectrometer in dual-inlet mode. Two splits of the in-house standard MON GT (5.38 ‰, Harris and Vogeli, 2010) were analyzed with each batch of 10 samples, and the values obtained for MON GT were used to recalculate raw data to the SMOW scale. The long-term average difference in $\delta^{18}O$ values of duplicates of MON GT is 0.12 ‰, which corresponds to a 2σ value of 0.16 ‰ (n=283).

RESULTS

Petrography

a. Airekan Granite

Airekan granite is a pink to red color fractured intrusion. The primary mineral parageneses in Airekan granite are including around 35 vol% of quartz, ~45 vol% of alkali-feldspars, ~5-15 vol% of biotite, ~5-10 vol% of primary sub- to euhedral muscovite (Ms_1), ~10> vol% of plagioclases, and accessory minerals of zircon, apatite, rutile, and opaque minerals (Figure 2 c,d,e). Zircon with pleochroic halo is a common inclusion within

Table 1. Average EPMA data of minerals in Airekan granite and related aplitic dikes and enclave (north of Yazd Block, CEIM) (Main oxide contents in wt% were recast in mineral composition formula in atoms per formula unit (a.p.f.u.) following guidelines of Papike (1988) and the appendices in Deer et al (2013).

Mineral type	Alkali Feldspar			Plagioclase				Biotite			Muscovite		
Rock Type	Granite	Aplitic Dike	Enclave	Granite	Enclave	Granite	Aplitic Dike	Granite	Aplitic Dike	Enclave	Granite	Aplitic Dike	Enclave
Sample No.	GR4, GR8, GR9	AD3, AD1	EN1	GR4, GR8, GR9	EN1	GR4	AD3, AD1	GR4, GR8, GR9	AD1, AD3	EN1	GR4, GR9	AD1	EN1
N (Point counts)	12	7	2	8	3	2	6	6	4	4	6	3	4
SiO_2	64.46	64.89	65.13	64.24	63.51	67.78	66.86	36.00	36.21	36.45	46.66	47.58	47.28
TiO_2	0.01	0.00	0.00	0.01	0.00	0.00	0.00	2.76	2.49	2.76	0.59	0.59	0.91
Al_2O_3	18.40	18.43	18.49	22.39	22.80	20.30	20.91	16.24	17.65	16.57	30.17	31.66	30.87
Cr_2O_3	0.00	0.00	0.00	0.00	0.00	0.00	0.00	0.02	0.01	0.01	0.00	0.01	0.01
FeO*	0.05	0.02	0.05	0.03	0.09	0.04	0.03	24.40	24.16	23.21	3.92	3.18	3.06
MnO	0.01	0.00	0.00	0.01	0.01	0.02	0.00	0.26	0.34	0.17	0.03	0.02	0.02
MgO	0.00	0.00	0.00	0.01	0.01	0.01	0.01	6.44	5.75	7.14	1.49	1.56	1.46
CaO	0.01	0.01	0.01	3.34	3.66	0.73	1.32	0.02	0.03	0.00	0.03	0.03	0.01
Na_2O	0.60	0.58	0.60	9.73	9.25	11.25	10.84	0.12	0.11	0.07	0.31	0.30	0.29
K_2O	16.69	16.80	15.74	0.15	0.68	0.25	0.13	9.90	9.58	9.80	11.16	11.59	10.80
Total	100.23	100.73	100.02	99.89	100.00	100.35	100.10	96.17	96.32	96.18	94.36	96.50	94.69
Oxygen No.	8	8	8	8	8	8	8	22	22	22	22	22	22
Si	2.99	2.99	3.00	2.84	2.81	2.96	2.93	5.57	5.55	5.57	6.39	6.35	6.41
Ti	0.00	0.00	0.00	0.00	0.00	0.00	0.00	0.32	0.29	0.32	0.06	0.06	0.10
Al^{Total}	1.00	1.00	1.00	1.16	1.19	1.04	1.08	2.96	3.19	2.99	4.87	4.98	4.93
Al^{IV}								2.43	2.45	2.43	1.61	1.65	1.60
Al^{VI}								0.54	0.74	0.56	3.27	3.33	3.33
Cr								0.00	0.00	0.00	0.00	0.00	0.00
Fe^{Total}								3.16	3.10	2.97	0.45	0.36	0.34
Fe^{3+}													
Fe^{2+}	0.00	00.00	00.00	0.00	0.00	0.00	0.00						
Mn								0.04	0.05	0.03	0.01	0.00	0.00
Mg								1.49	1.32	1.63	0.31	0.31	0.29
Ca	0.00	0.00	0.00	0.16	0.17	0.03	0.06	0.00	0.01	0.00	0.00	0.01	0.00
Na	0.05	0.05	0.05	0.83	0.79	0.95	0.92	0.04	0.03	0.02	0.08	0.08	0.08
K	0.99	0.99	0.93	0.01	0.04	0.01	0.01	1.96	1.88	1.92	1.96	1.98	1.87
Total	5.03	5.03	4.99	5.00	5.01	5.00	5.00	15.53	15.40	15.43	14.12	14.12	14.01
Anorthite (mole%)	0.05	0.05	0.05	15.81	17.26	3.41	6.26						
Albite (mole%)	5.18	4.98	5.47	83.34	78.93	95.19	93.01						
Orthoclase (mole%)	94.77	94.97	94.48	0.85	3.82	1.39	0.73						
Fe/Fe+Mg								0.68	0.71	0.65	0.60	0.53	0.54
X_{Ms}^{ideal}											0.51	0.52	
X_{Pg}^{ideal}											0.01	0.01	
X_{MgCel}^{ideal}											0.20	0.22	
X_{FeCel}^{ideal}											0.29	0.26	
Mineral Name	Orthoclase			oligoclase		albite		Annite			Muscovite		

Table 2. EPMA and LA-ICP-MS data of some minerals from Airekan granite and related aplitic dikes (north of Yazd Block, CEIM) (DL: detection limit; oxides are in wt%, elements are in ppm; Eu/Eu*: $Eu_n/(Sm_n.Gd_n)^{0.5}$; chondrite normalization factor from: McDonough and Sun, 1995).

Rock Type	Granite				Aplitic Dike			
Sample No.	GR4				AD3			
Point No. (EPMA)	77		85		108		109	
Mineral Type	Orthoclase	DL	Oligoclase	DL	Orthoclase	DL	Albite	DL
SiO_2	65.22	0.01	65.59	0.01	65.20	0.01	66.14	0.01
TiO_2	0.00	0.01	0.00	0.01	0.00	0.01	0.00	0.01
Al_2O_3	18.48	0.01	21.61	0.01	18.44	0.01	21.00	0.01
Cr_2O_3	0.00	0.01	0.00	0.01	0.00	0.01	0.00	0.01
FeO*	0.01	0.01	0.03	0.01	0.02	0.01	0.09	0.01
MnO	0.01	0.01	0.01	0.01	0.01	0.01	0.01	0.01
MgO	0.01	0.01	0.00	0.01	0.00	0.01	0.01	0.01
CaO	0.00	0.01	2.56	0.01	0.00	0.01	1.89	0.01
Na_2O	0.50	0.01	10.33	0.01	0.73	0.01	10.93	0.01
K_2O	15.89	0.01	0.25	0.01	15.69	0.01	0.11	0.01
NiO	0.00	0.01	0.00	0.01	0.00	0.01	0.00	0.01
Total	100.11	0.01	100.38	0.01	100.10	0.01	100.19	0.01
Ca $_{(calculated)}$	627	185	16193	214	685	179		
Ti $_{(calculated)}$	4.4	1.02	4.8	0.89	8.8	0.92		
Point No. (LA-ICP-MS)	403		404		501		502	
Rb	412.8	0.08	0.5	0.10	391.7	0.07	0.1	0.06
Sr	94.54	0.02	146.02	0.01	99.21	0.02	106.52	0.01
Y	0.072	0.02	0.054	0.01	0.171	0.03	2.414	0.02
Ba	943.5	0.11	9.2	0.18	200.3	0.15	1.5	0.09
La	0.012	0.01	0.030	0.01	0.123	0.01	2.031	0.01
Ce	0.010	0.01	0.047	0.01	0.030	0.01	4.361	0.01
Pr	-	0.02	-	0.01	0.030	0.01	0.38	0.02
Nd	-	0.07	-	0.06	-	0.07	1.531	0.08
Sm	-	0.07	-	0.07	-	0.08	0.543	0.09
Eu	0.096	0.03	0.079	0.02	0.222	0.03	0.16	0.02
Gd	-	0.10	-	0.11	-	0.07	0.384	0.08
Tb	-	0.01	-	0.02	-	0.01	0.094	0.01
Dy	-	0.07	-	0.06	-	0.05	0.574	0.04
Ho	-	0.02	-	0.02	-	0.02	0.104	0.01
Er	-	0.04	-	0.03	-	0.04	0.240	0.03
Tm	-	0.02	-	0.01	-	0.02	0.031	0.02
Yb	-	0.06	-	0.07	-	0.05	0.126	0.04
Lu	-	0.01	-	0.03	-	0.02	0.384	0.03
Ta	0.073	0.03	-	0.03	0.036	0.03	-	0.03
Pb	52.76	0.15	17.73	0.15	68.34	0.18	14.321	0.16
Th	-	0.05	-	0.03	-	0.05	0.089	0.03
U	-	0.03	-	0.05	-	0.04	0.261	0.02
Eu/Eu*	-		-		-		1.07	
La_n/Yb_n	-		-		-		10.91	
La_n/Sm_n	-		-		-		2.34	
Gd_n/Yb_n	-		-		-		2.46	

Table 3. XRF, ICP-MS and gravimetric analysis of Airekan granite and related aplitic dikes and mafic enclave (north of Yazd Block, CEIM) (oxides and LOI are in wt%, elements are in ppm; *: NAA data by the second author; DL: detection limits).

Rock Type			Granite									
Sample No.	Method	DL	G13	G6	G18	G10	G17	G4	G19	G12	G2	G14
SiO_2	XRF	0.5	70.10	72.44	72.95	73.08	73.22	73.50	73.98	77.12	77.20	77.99
TiO_2	XRF	0.01	0.44	0.24	0.30	0.32	0.31	0.30	0.24	0.08	0.18	0.15
Al_2O_3	XRF	0.1	14.29	14.25	13.89	14.33	13.57	13.18	13.46	12.56	11.95	11.62
$Fe_2O_3^{total}$	XRF	0.1	3.31	1.56	2.10	2.34	2.45	2.21	1.90	0.54	1.69	1.29
MnO	XRF	0.005	0.026	0.021	0.018	0.033	0.025	0.023	0.022	<0.01	0.023	<0.01
MgO	XRF	0.01	0.77	0.27	0.49	0.53	0.50	0.51	0.44	0.07	0.26	0.16
CaO	XRF	0.01	1.55	1.49	1.50	1.26	1.01	1.33	1.11	0.55	1.07	0.95
Na_2O	XRF	0.01	2.81	3.06	3.38	4.00	2.81	2.94	3.08	2.50	2.84	2.67
K_2O	XRF	0.05	4.74	5.48	3.93	3.72	5.20	4.68	4.92	6.17	4.26	4.40
P_2O_5	XRF	0.01	0.11	0.06	0.08	0.09	0.08	0.08	0.06	0.02	0.05	0.04
LOI	gravimetry		1.73	1.33	1.35	0.49	0.77	1.32	0.89	0.58	0.76	0.83
Total	-		99.9	100.2	100.0	100.2	100.0	100.1	100.1	100.2	100.3	100.1
A/CNK	-		1.14	1.04	1.11	1.11	1.12	1.07	1.08	1.07	1.06	1.07
A/NK	-		1.47	1.30	1.42	1.35	1.32	1.33	1.30	1.16	1.29	1.27
K/(Na+K)	-		0.65	0.67	0.57	0.51	0.67	0.64	0.64	0.73	0.63	0.65
Q	CIPW		31.47	30.25	34.53	32.34	34.31	35.11	34.38	37.75	41.84	43.46
Or	CIPW		28.01	32.39	23.23	21.98	30.73	27.66	29.08	36.46	25.18	26.00
Ab	CIPW		23.78	25.89	28.60	33.85	23.78	24.88	26.06	21.15	24.03	22.59
An	CIPW		6.95	6.99	6.93	5.68	4.46	6.09	5.11	2.59	5.01	4.48
C	CIPW		1.99	0.72	1.54	1.64	1.68	1.05	1.20	0.82	0.83	0.82
Hy	CIPW		1.92	0.67	1.22	1.32	1.25	1.27	1.10	0.17	0.65	0.40
Ru	CIPW		0.41	0.21	0.28	0.28	0.28	0.27	0.21	0.08	0.16	0.15
Ap	CIPW		0.27	0.14	0.19	0.21	0.20	0.19	0.14	0.05	0.11	0.09
Il	CIPW		0.06	0.05	0.04	0.07	0.05	0.05	0.05	0.00	0.05	0.00
Li	ICP-MS	0.21	26.5	8.3	22.3	17.0	21.3	24.9	15.8	2.1	6.5	5.7
Be	ICP-MS	0.1	4.9	2.4	4.6	3.0	3.6	3.2	3.5	2.2	3.0	6.6
Sc	ICP-MS	0.5	12.8	10.8	11.3	11.3	10.8	12.4	10.9	8.9	11.4	10.7
Ti	ICP-MS	0.001	0.26	0.14	0.18	0.19	0.19	0.18	0.14	0.05	0.11	0.09
V	ICP-MS	0.5	33.0	15.2	20.4	21.0	20.6	21.2	15.7	4.0	10.7	8.0
Cr	ICP-MS	0.5	20.7	10.4	15.6	12.8	13.8	14.7	12.5	14.0	12.4	10.7
Co	ICP-MS	0.5	3.96	1.39	2.20	2.79	4.65	2.45	2.07	0.86	1.85	1.08
Ni	XRF	5	<10	<10	123.0	<10	<10	<10	<10	<10	<10	<10
Cu	XRF	5	<10	<10	32	<10	14	<10	<10	<10	<10	<10
Zn	XRF	5	31	14	121	37	32	22	19	<10	20	<10
Ga	ICP-MS	1	18.9	17.3	18.3	17.8	17.5	17.3	16.3	12.9	15.5	15.4
Rb	ICP-MS	1	218	192	163	99	192	184	179	186	152	180
Sr	XRF	5	467	178	60	226	255	319	124	127	81	95
Y	ICP-MS	0.01	39.0	32.5	44.3	27.2	39.9	31.6	34.0	24.5	42.6	41.6
Zr	XRF	5	210	137	47	174	149	146	123	52	118	83
Nb	XRF	5	15	14	14	16	15	15	12	<10	14	13
Ba**	NAA	40	747	376	325	620	-	348	-	-	-	266
Mo	ICP-MS	0.1	1.28	0.58	0.55	0.37	0.76	0.69	0.46	0.59	0.94	0.83
Cs	ICP-MS	0.5	7.21	3.36	4.15	2.11	4.89	4.22	4.07	1.72	2.37	1.80
La	ICP-MS	0.1	42.8	41.1	34.8	36.1	41.6	37.2	38.4	23.3	33.1	29.1
Ce	ICP-MS	0.1	84	86	70	68	78	77	79	48	69	62

Table 3. Continued ...

Rock Type			Granite									
Sample No.	Method	DL	G13	G6	G18	G10	G17	G4	G19	G12	G2	G14
Pr	ICP-MS	0.02	9.96	9.51	8.00	7.59	9.70	8.53	9.09	5.54	7.74	7.44
Nd	ICP-MS	0.04	38	35	30	27	36	32	33	20	29	28
Sm	ICP-MS	0.01	7.41	7.04	6.13	5.24	7.50	6.62	6.73	4.05	6.40	6.24
Eu	ICP-MS	0.05	0.940	0.657	0.657	0.820	0.766	0.650	0.634	0.400	0.336	0.328
Gd	ICP-MS	0.08	6.67	6.11	5.74	4.68	6.89	6.02	6.07	3.53	5.89	5.93
Tb	ICP-MS	0.003	1.13	1.01	1.05	0.78	1.21	1.02	1.04	0.63	1.12	1.14
Dy	ICP-MS	0.04	6.72	5.69	6.53	4.57	6.97	5.77	5.91	3.88	6.94	6.76
Ho	ICP-MS	0.008	1.31	1.11	1.45	0.92	1.36	1.08	1.16	0.79	1.44	1.39
Er	ICP-MS	0.03	3.70	2.99	4.49	2.62	3.73	2.80	3.05	2.22	4.30	4.13
Tm	ICP-MS	0.005	0.567	0.455	0.711	0.399	0.529	0.388	0.429	0.356	0.683	0.657
Yb	ICP-MS	0.04	3.72	2.91	4.65	2.62	3.24	2.38	2.56	2.37	4.65	4.41
Lu	ICP-MS	0.003	0.568	0.440	0.680	0.407	0.463	0.361	0.359	0.360	0.701	0.647
Ta	ICP-MS	0.5	1.37	0.94	1.07	0.86	1.12	1.03	0.87	0.88	1.30	2.10
Pb	XRF	5	21	21	<10	19	20	24	26	20	21	18
Th	ICP-MS	0.5	22.0	22.4	19.4	17.8	20.4	22.1	20.2	14.7	21.2	20.9
U	ICP-MS	0.5	2.00	1.52	1.38	1.96	1.69	1.40	1.05	1.09	2.97	3.48
Ba/Pb	-		35.57	17.90	-	32.63	-	14.50	-	-	-	14.78
Th/U	-		11.0	14.7	14.1	9.1	12.1	15.8	19.2	13.5	7.1	6.0
Th/Ta	-		16.06	23.83	18.13	20.70	18.21	21.46	23.22	16.70	16.31	9.95

Rock Type			Aplitic Dike				Enclave	
Sample No.	Method	DL	AD9	AD3	AD8	AD1	EN1	A29*
SiO_2	XRF	0.5	69.20	72.54	76.96	77.57	67.57	67.98
TiO_2	XRF	0.01	0.38	0.06	0.10	0.08	0.58	0.28
Al_2O_3	XRF	0.1	15.60	12.83	12.07	12.37	15.07	15.02
$Fe_2O_3^{total}$	XRF	0.1	3.15	3.23	1.06	0.57	4.56	4.55
MnO	XRF	0.005	0.032	0.053	<0.01	<0.01	0.042	0.040
MgO	XRF	0.01	0.96	0.21	0.09	0.06	1.14	1.38
CaO	XRF	0.01	1.77	1.04	0.79	0.69	2.01	1.51
Na_2O	XRF	0.01	3.95	2.95	2.61	2.82	3.56	3.94
K_2O	XRF	0.05	3.86	5.83	5.55	5.47	4.43	3.96
P_2O_5	XRF	0.01	0.12	0.09	0.03	0.02	0.15	-
LOI	gravimetry		1.04	1.07	0.68	0.54	0.86	1.35
Total	-		100.1	99.9	99.9	100.2	100.0	100.0
A/CNK	-		1.12	0.98	1.03	1.05	1.05	1.11
A/NK	-		1.46	1.15	1.17	1.17	1.41	1.39
K/(Na+K)	-		0.52	0.69	0.70	0.68	0.58	0.53
Q	CIPW		26.58	30.80	38.80	38.73	24.32	24.62
Or	CIPW		22.81	34.45	32.80	32.33	26.18	23.40
Ab	CIPW		33.42	24.96	22.09	23.86	30.12	33.34
An	CIPW		7.98	4.55	3.73	3.29	9.01	7.49
C	CIPW		2.00	0.00	0.40	0.60	1.12	1.51
Hy	CIPW		2.39	0.52	0.22	0.15	2.84	3.44
Ru	CIPW		0.35	0.00	0.10	0.08	0.53	0.23
Ap	CIPW		0.29	0.22	0.07	0.05	0.35	0.00
Il	CIPW		0.07	0.11	0.00	0.00	0.09	0.09

Table 3. Continued ...

Rock Type			Aplitic Dike				Enclave	
Sample No.	Method	DL	AD9	AD3	AD8	AD1	EN1	A29*
Li	ICP-MS	0.21	31.4	3.7	2.2	0.9	53.1	-
Be	ICP-MS	0.1	5.8	5.6	2.1	3.2	5.9	-
Sc	ICP-MS	0.5	12.9	9.2	10.1	9.9	13.2	10
Ti	ICP-MS	0.001	0.23	0.04	0.06	0.05	0.35	-
V	ICP-MS	0.5	18.3	3.5	3.0	2.9	41.4	44
Cr	ICP-MS	0.5	7.2	14.4	15.2	11.3	22.3	-
Co	ICP-MS	0.5	4.14	2.24	0.68	0.48	6.20	7
Ni	XRF	5	<10	<10	<10	<10	<10	-
Cu	XRF	5	<10	<10	<10	<10	<10	-
Zn	XRF	5	45	22	<10	<10	61	55
Ga	ICP-MS	1	21.7	13.4	14.7	14.5	20.6	-
Rb	ICP-MS	1	174	173	173	162	248	295
Sr	XRF	5	414	77	491	117	207	-
Y	ICP-MS	0.01	34.8	68.1	31.0	29.7	37.8	47
Zr	XRF	5	309	47	66	56	355	-
Nb	XRF	5	17	13	10	<10	19	-
Ba**	NAA	40	-	344	114	178		-
Mo	ICP-MS	0.1	0.31	0.59	0.62	0.36	0.49	-
Cs	ICP-MS	0.5	5.66	1.71	1.73	1.26	8.20	8.96
La	ICP-MS	0.1	38.3	12.0	71.9	24.6	50.5	51.34
Ce	ICP-MS	0.1	79	27	152	54	99	84
Pr	ICP-MS	0.02	9.04	3.21	17.62	6.22	11.19	-
Nd	ICP-MS	0.04	33	13	64	23	42	38
Sm	ICP-MS	0.01	7.24	4.03	11.36	5.19	7.99	6.57
Eu	ICP-MS	0.05	0.554	0.332	0.232	0.174	0.810	1.16
Gd	ICP-MS	0.08	6.46	5.44	8.35	4.65	6.98	5.79
Tb	ICP-MS	0.003	1.11	1.25	1.17	0.86	1.14	1.12
Dy	ICP-MS	0.04	6.32	8.97	5.83	5.05	6.47	7.1
Ho	ICP-MS	0.008	1.21	2.09	1.05	1.02	1.30	1.54
Er	ICP-MS	0.03	3.31	6.90	2.66	2.90	3.63	-
Tm	ICP-MS	0.005	0.501	1.150	0.381	0.458	0.550	0.72
Yb	ICP-MS	0.04	3.21	8.10	2.46	3.10	3.54	4.39
Lu	ICP-MS	0.003	0.477	1.268	0.373	0.463	0.525	0.7
Ta	ICP-MS	0.5	1.15	2.74	0.74	1.79	1.26	1.53
Pb	XRF	5	11	35	23	28	12	-
Th	ICP-MS	0.5	17.3	13.0	62.1	18.7	18.0	17.13
U	ICP-MS	0.5	1.57	4.00	1.76	2.84	3.66	-
Ba/Pb	-		-	9.83	4.96	6.36	-	-
Th/U	-		11.0	3.3	35.3	6.6	4.9	-
Th/Ta	-		15.04	4.74	83.92	10.45	14.29	11.20

biotites. The other common inclusions are tiny prismatic crystals of apatite. Subhedral crystals of muscovite, fine-grained sericite, and clay minerals are the secondary phases. The small crystals (~0.1 mm) of secondary muscovites (Ms_2) are formed at the expense of aluminous phases (e.g., feldspar and micas). The feldspars are also sericitized to some extent. The common microscopic textures of Airekan granite are medium to coarse-grained

Table 4. Th+U content (in ppm) and $^{206}Pb/^{238}U$ ratios of representative zircons in Airekan pluton (Note: adopted from Shirdashtzadeh et al. (2018); Zircon crystallization phase: S=inherited; I=magmatic; M=metamorphic).

Analysis No.	Th (ppm)	U (ppm)	Th+U (ppm)	$^{206}Pb/^{238}U$ ratio	1σ	Zircon Type
IR-1	178.32	456.21	634.52	0.0831	0.0009	I
IR-03	427.83	813.73	1241.56	0.0835	0.0010	I
IR-05	135.52	491.28	626.80	0.0806	0.0009	I
IR-06	264.31	1108.14	1372.45	0.0669	0.0007	M
IR-07	197.93	1661.28	1859.21	0.0633	0.0007	M
IR-08	163.95	730.60	894.56	0.1111	0.0013	S
IR-09	347.34	1511.36	1858.71	0.0606	0.0007	M
IR-11	290.65	755.72	1046.37	0.0721	0.0008	I
IR-12	354.97	1560.54	1915.52	0.0605	0.0008	M
IR-13	805.59	1161.11	1966.70	0.0613	0.0008	M
IR-14	138.74	511.61	650.36	0.0762	0.0010	I
IR-15	186.46	258.26	444.73	0.0898	0.0011	S
IR-16	1032.61	1595.09	2627.69	0.0524	0.0006	M
IR-18	310.52	1738.18	2048.70	0.0638	0.0007	M
IR-19	347.24	1123.14	1470.38	0.0789	0.0009	M
IR-20	410.88	1090.79	1501.67	0.0744	0.0008	I
IR-22	399.08	595.16	994.24	0.0807	0.0010	I
IR-24	238.60	614.86	853.45	0.1484	0.0016	S
IR-28	914.88	818.41	1733.29	0.0754	0.0009	I
IR-30	319.60	1117.08	1436.68	0.0765	0.0008	I
IR-38	151.04	456.22	607.26	0.0786	0.0009	I
IR-39	220.04	291.96	512.00	0.0999	0.0012	S
IR-49	214.23	841.78	1056.01	0.0773	0.0009	I
IR-56	360.55	1110.13	1470.68	0.0667	0.0008	M
IR-57	166.28	503.51	669.79	0.0841	0.0009	I
IR-65	197.96	992.86	1190.82	0.0837	0.0010	I
IR-72	918.19	1252.88	2171.07	0.0800	0.0009	I
IR-73	369.19	715.73	1084.92	0.0769	0.0009	I
IR-74	584.32	1640.46	2224.77	0.0595	0.0007	M
IR-77	446.29	2719.97	3166.26	0.0445	0.0005	M
IR-85	239.15	837.76	1076.92	0.0731	0.0009	I
IR-87	515.57	716.03	1231.60	0.0840	0.0010	I
IR-90	214.49	1660.71	1875.20	0.0790	0.0010	I
IR-93	165.25	669.99	835.23	0.0776	0.0009	I
IR-95	154.56	989.95	1144.52	0.0731	0.0009	I
IR-100	261.43	1779.83	2041.25	0.0587	0.0007	M

xenomorphic granular and pertithic (Figure 2); however, deformation and mylonitic textures and microstructures are also occurred as a record of tectonic evolution. For example, foliation with alternating bands of felsic and mafic minerals are seen in both scales of hand specimen (Figure 2f) and thin sections. The microscopic signatures of ductile deformations are including quartz with undulose extinction (Figure 2g) and GBM recrystallization and lobate margins (Figure 2g), as well as feldspars with BLG recrystallization (Figure 2c), flame perthite (Figure

Table 5. $\delta^{18}O$ values of quartz grains from granite and aplitic dikes of Airekan.

Sample No.	Rock Type	$\delta^{18}O$ of Quartz	$\delta^{18}O$ of Rock *
GR1	granite	12.24	11.13
GR2	granite	12.17	11.06
GR4	granite	12.36	11.25
GR5	granite	12.18	11.07
GR8	granite	11.07	9.96
GR9	granite	11.45	10.34
GR10	granite	11.28	10.17
GR12	granite	12.10	10.99
Average		11.86	10.75
AD1	Aplite dike	12.71	11.60
AD3	Aplite dike	11.71	10.60
AD9	Aplite dike	12.41	11.30
Average		12.28	11.17

2c), kinking (Figure 2c), myrmekite (Figure 2h), and microcline formation during deformation and cooling of the granitic pluton (Figure 2i). According to Passchier and Trouw (2005), these textural features resemble a deformation stage at about 500-600 °C. At this condition, the biotites generally show cataclastic deformation.

b. Crosscutting aplitic dikes

Abundant fine-grained light-colored aplitic dikes dissect the Airekan granite in approximately N-E direction (Figure 3a). The aplitic dikes crosscuting the common foliation of host rock (Figure 3a) indicate further injection of aplitic magma into the cooled and fractured granitic intrusion. They are one to 50 cm in width with sharp margins with no compositional and textural alteration toward the host rock. The aplitic dikes are comparable with the host granite in modal composition. Mineralogically, they are composed of primary phases of small (~<1 mm) sub- to anhedral crystals of alkali-feldspar, quartz, biotite, muscovite, and minor amount of plagioclase (Figure 3 b,c). The accessory minerals are zircon, apatite, and opaque minerals. Clay minerals are the most common secondary phases. The aplitic dikes are very fine-grained and show aplitic and xenomorphic granular textures (Figures 3 b,c). They show some feature of deformed rocks. For example, feldspars rarely show deformation twinning (Figure 3c) and quartz grains with undulose extinction and lobate margins are indicative of GBM recrystallization (Figure 3b). However, flame perthite and myrmekite are not common. According to Passchier and Trouw (2005), these microstructural features indicate a mylonitization stage occurred at lower temperature (i.e., ~500 °C) than the granitic host rock.

c. Enclaves

Airekan intrusion also contains some dark-colored, fine-grained rounded enclaves, which are up to 0.5 m in size (Figure 3d). Microscopic observations (Figure 3 e,f) indicate they are similar to the granitic host rock in mineralogy, but comparatively they contain fairly higher modal content of biotite (~35 vol%) and lower modal content of quartz (Figure 3e). According to classification by Didier and Barbarin (1991), the petrographic feature of Airekan enclaves (e.g., ellipsoidal shape of enclaves, sharp contact with host rock in the margins of enclaves, igneous fine-grained texture, absence of silimanite and garnet, and the more abundant hydrous mafic mineral of biotite; Figure 3e) are indicative of 'microgranular enclave' formed by melts originated from deep crust.

EMPA of minerals

The average composition of minerals is presented in Table 1. In the case of granite samples, the alkali-feldspars are orthoclase, while the plagioclases are albite-oligoclase (Figure 4a). The biotite are annite with TiO_2 ~2.76 wt% and Fe# ~0.68 (Table 1; Figure 4b). The primary muscovites have X_{Ms}^{ideal} ~0.51 (Table 1). In comparison, enclave contains alkali-feldspars with orthoclase composition, while the plagioclases are more calcic (i.e., oligoclase) (Figure 4a). Their biotites are annite with lower Fe/(Fe+Mg) content (Figure 4b). In the aplitic dikes, alkali-feldspars are microcline and orthoclase, while the plagioclases are albite in composition (Figure 4a). The biotite is annite (Table 1; Figure 4b).

LA-ICP-MS of feldspar

Trace and rare earth elements chemistry of feldspar in granite and aplitic rocks (Table 2) are shown on the primitive mantle normalized diagram in order to make a better comparison among the samples (Figure 5a). REE contents of feldspar samples are lower than detection limits (except for albite in aplitic dike which shows relatively higher LREE/HREE content), but other analyzed elements are higher in plagioclase than alkali-feldspar (Figure 5a). The feldspars are characterized by enrichment in Rb, K, Pb, Sr contents and slightly higher LREE abundant (Figure 5a).

Whole rock chemistry

The Airekan samples are exclusively felsic in composition without any intermediate to mafic varieties. They are granite based on their normative composition (Figure 5b). The SiO_2 content (granite ~ 70-78 wt%, aplitic dikes ~69-77 wt%, enclave ~67 wt%) shows their acidic and granitic nature (Table 3) and high-K calc-alkaline affinity. They are low to intermediate peraluminous to felsic peraluminous with alumina saturation index (ASI) >1 (A/CNK>1) and

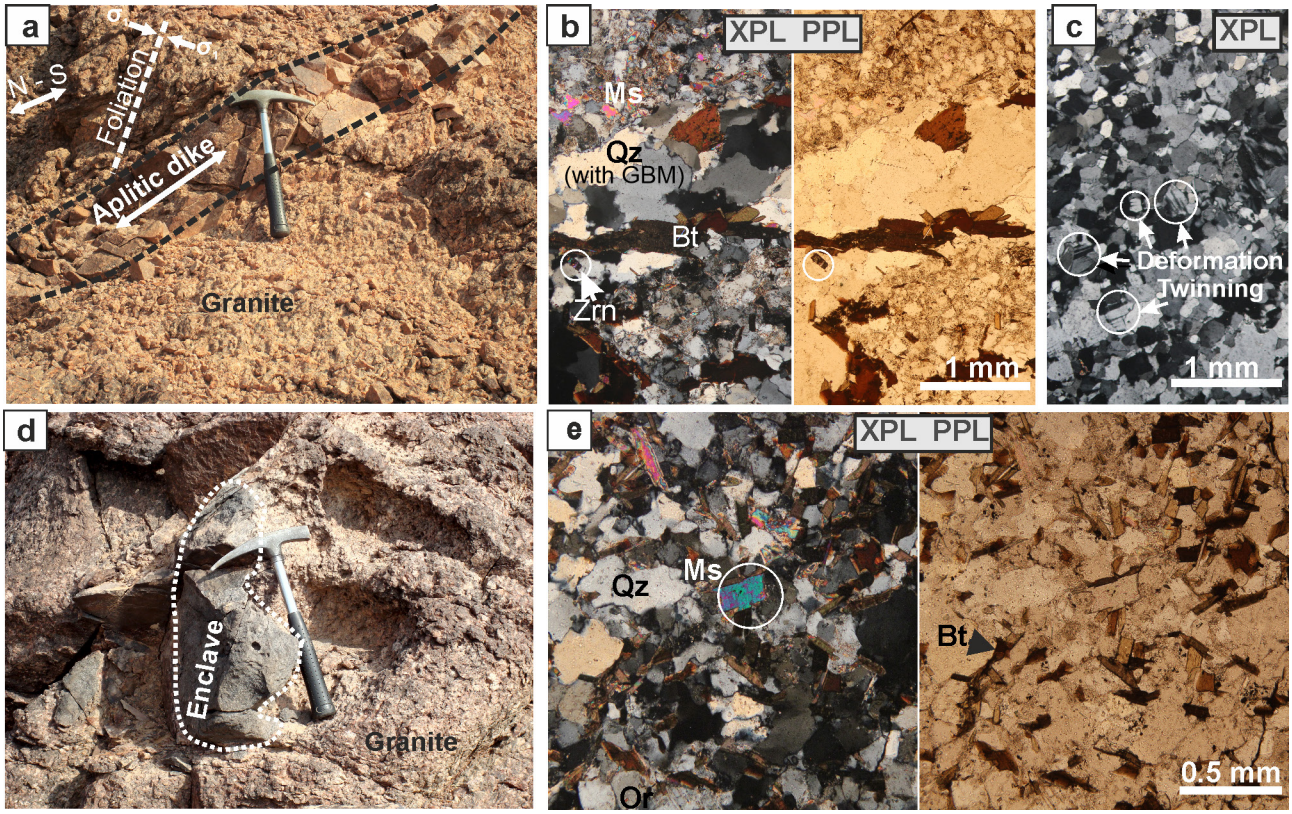

Figure 3. (a) The granitic intrusion of Airekan (north of Yazd Block, CEIM) dissect by aplitic dikes; (b) Photomicrograph of common mineralogy and partially deformed granular texture in an aplitic dike; (c) Photomicrograph of deformation twinning developed in some feldspars; (d) Dark-coloured fine-grained ellipsoidal enclaves within the granitic intrusion; (e) Photomicrograph of common mineralogy and fine-grained igneous texture of an enclave.

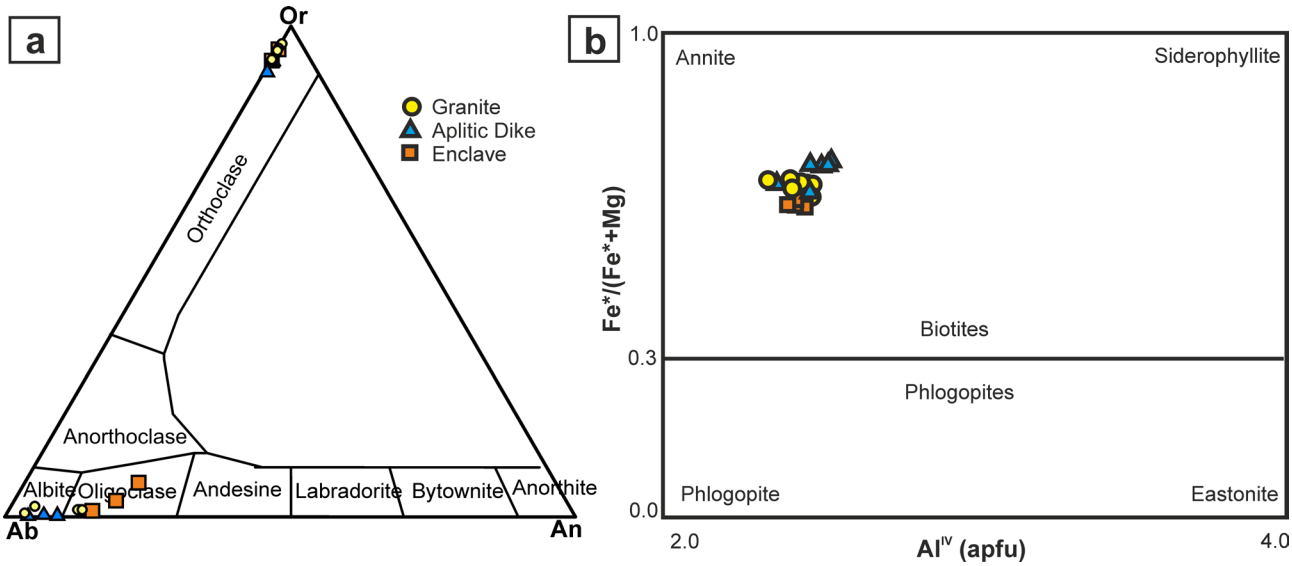

Figure 4. (a) Feldspar ternary classification diagram (Deer et al., 1992); (b) Biotite classification diagram (Deer et al., 1992).

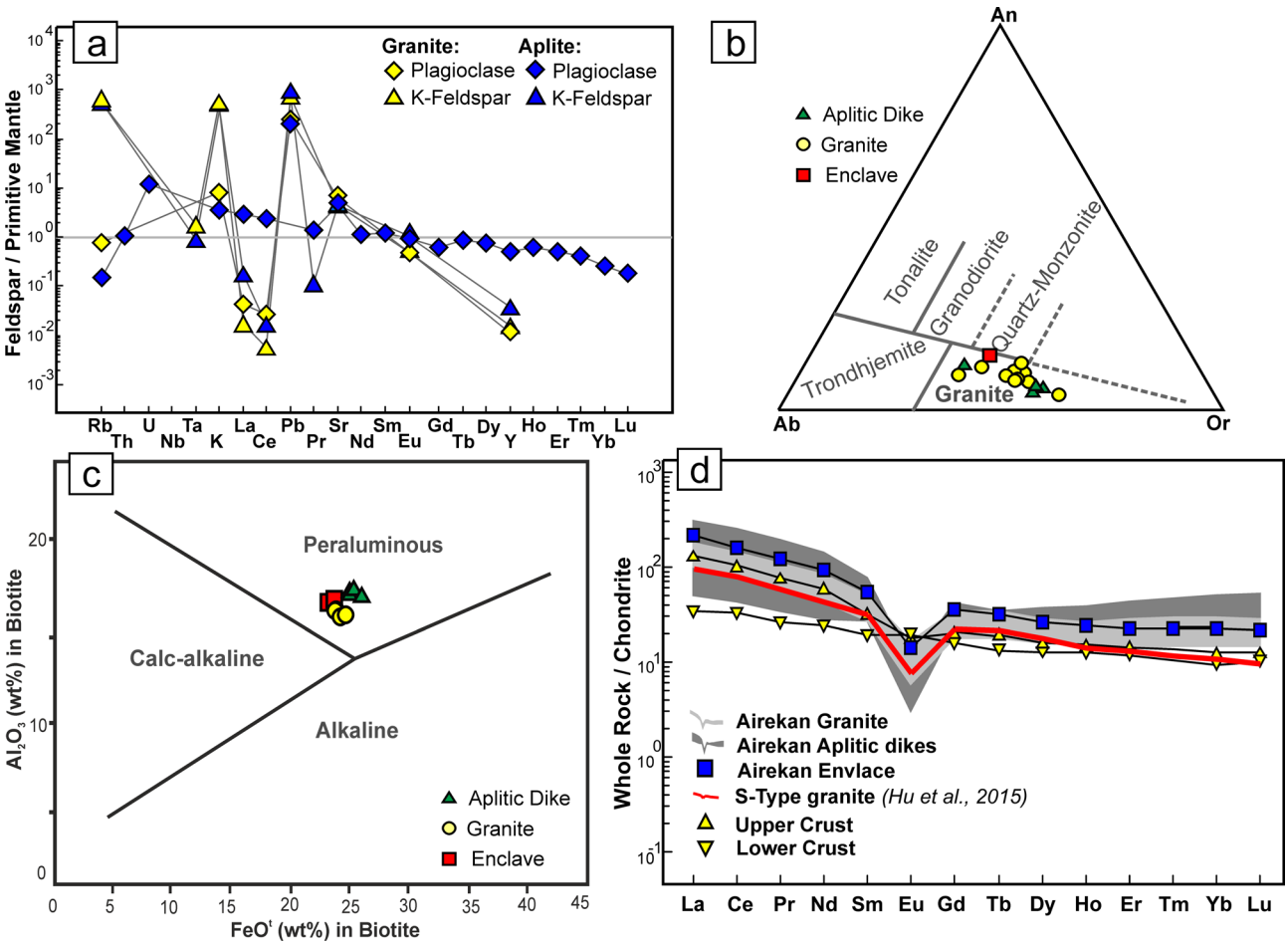

Figure 5. (a) Primitive mantle-normalized patterns for feldspar in granite (sample GR4) and aplitic dike (sample AD3); (b) Normative An-Ab-Or ternary diagram (after O'Connor, 1965); (c) Biotite composition in Airekan granite and associated igneous rocks on the MgO-Al_2O_3-FeO ternary discriminant plot (Abdel-Rahman, 1994); (d) Chondrite-normalized pattern for whole rock composition of granite and aplitic dike samples (samples GR4 and AD3). Normalization values for primitive mantle and chondrite are from McDonough and Sun (1995). Compositions of upper and lower crusts are from Taylor and McLennan (1981).

A/NK>1 (Table 3). In addition, composition of biotite confirms a peraluminous magma (Figure 5c). The granite, aplitic dikes and the enclave are similarly characterized by slightly high LREE contents (La_n/Yb_n of ~4.5-10.6 for granite and aplitic dikes; Table 3), negative Eu anomaly and slightly depletion in HREE (Figure 5d).

Isotopic ratios for quartz and zircon

Under cathodoluminescence images with high quality resolution, the prismatic grains of zircons in Airekan granite mostly show oscillatory zoning characterizing the magmatic zircons; however, some grains record a more complex history. As shown in Figure 6a, they contain rounded unzoned inherited cores (phase 1), covered by a brighter outer magmatic overgrowth with oscillatory (phase 2) and then a darker recrystallized metamorphic overgrowth (phase 3). The isotopic ratio of $^{206}Pb/^{238}U$ and Th+U (in ppm) for different crystallization phases of zircon are presented in Table 4. $^{206}Pb/^{238}U$ is decreasing from phase 1 to 3, while Th+U is approximately increasing (Figure 6b).

In addition, the oxygen isotope data for quartz crystals are reported in the familiar δ notation where $\delta^{18}O=(R_{sample}/R_{standard}-1)*1000$ and $R=^{18}O/^{16}O$. It is from 11.07 to 12.36 ‰ with an average of 11.86 ‰ (n=8; 1σ = 0.5) for quartz crystals from the Airekan granite (Table 5). The crosscutting aplitic dikes show higher $\delta^{18}O$ values, ranging from 11.71 to 12.71 ‰ with an average of 12.28 ‰ (n=3; 1σ=0.5) (Table 5). The uniformity of composition suggests that all quartz share a common origin. On the other hand, the difference in $\delta^{18}O$ value between quartz in a granite and the original magma depends on rate of cooling, grain size, and choice of mineral magma fractionation factors. Fourie and Harris (2011) estimated that quartz had a $\delta^{18}O$

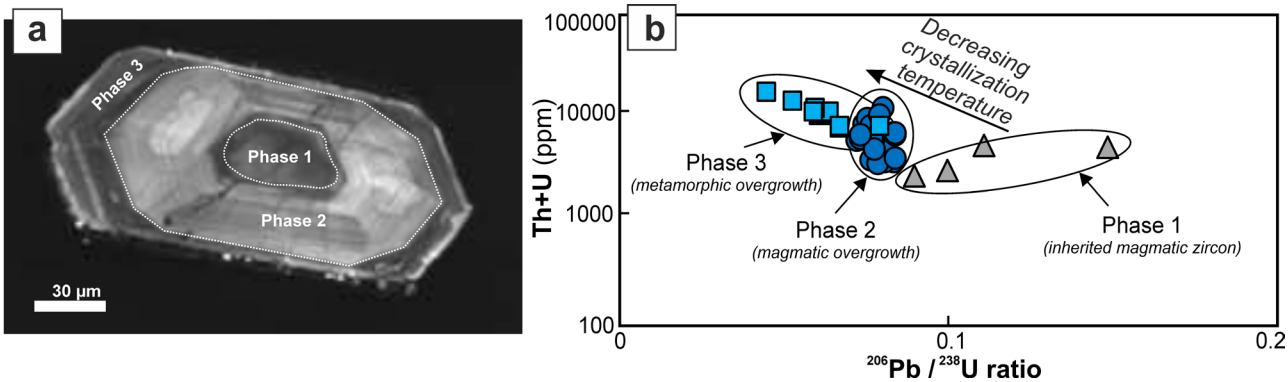

Figure 6. (a) Cathodoluminescence images of inherited core, magmatic, and metamorphic overgrowths of zircons from Airekan granite (north of Yazd Block, CEIM); (b) $^{206}Pb/^{238}U$ ratio versus Th+U (ppm) for the zircon grains.

value 1.11 ‰ higher than the magmas from which the Bushveld granites crystallized. Assuming similar values here, the Airekan granite and aplitic dikes crystallized from magmas having $\delta^{18}O$ values of 10.75‰ and 11.17 ‰, respectively (Table 5).

DISCUSSION

Granite classification

The studied samples in Airekan pluton are alkali-feldspar granite in modal composition. Considering the diagrams (not presented here) by Furnes et al. (1969) and Collins et al. (1982), they are distinct from A-type granite based on their average contents of calc-alkalic magnesian nature, $Na_2O+K_2O/CaO<10$, Y~40 ppm, Zr~140 ppm, Zn<121 ppm, Ce~76 ppm, Ga~17ppm, Al_2O_3~13.5wt%, and SiO_2~73wt%.

According to biotite composition (Figure 5c), the alumina saturation index (Table 3), and morphology of magmatic rims of zircon crystals (Shirdashtzadeh et al., 2018), Airekan granite and aplitic dikes are similar to peraluminous S-type rocks. Based on classification by Bell et al. (2017), high FeO*/MgO (~3.8-4.2) of biotites in granite and aplitic dikes indicates they are derived exclusively from ilmenite series sources (i.e., S-type granite); whereas lower FeO*/MgO of biotites in the enclave (~3.2) is closer to a magnetite series sources (i.e., I-type granite). Therefore, enclaves are similar to low-temperature I-type granites, which have originated from deeper crustal depths rather than anatexis of metasedimentary rocks, considering their igneous texture, absence of sillimanite and garnet, and approximately more mafic nature.

According to various classification schemes for granites, the chemical features that emphasize an S-type nature for the studied peraluminous granite and aplitic dikes are listed in the following:

(1) Indicator minerals of I-type granites (i.e., hornblende, magmatic sphene), and minerals which are expected in S-type granites (i.e., sillimanite, garnet, and cordierite) are absent from these rocks, however, biotite with high FeO/MgO and magmatic muscovite crystals are indicators of peraluminous and S-type granites;

(2) Based on Clemens (2003), the S-type granites commonly contain 'microgranular enclave' with igneous fine-grained texture and the more mafic nature (than the host rock), as is the case in Airekan granite.

(3) The SiO_2 content of the Airekan granite and aplitic rocks (>70 wt%) is similar to S-type (65-76 wt%) and I-type (53-76 wt%) granites. However, A/CNK, A/NK and the normative corundum values (~0.8-2; Table 3) are indicative of mildly to felsic peraluminous S-type granites. Na_2O/K_2O ratio almost resembles S-type nature for aplites and the host granite (Na_2O ~2.5 to 4 wt%), but I-type nature for the enclave samples (>3.2 wt%) (Figure 7a). Rb>~160 ppm, Y<50 ppm and Th<30 ppm contents of samples are comparable with S-type granites studied by Chappell (1999).

(4) The Airekan granite is relatively more enriched in Rb, Th, U, Nb, Pb, Ta, K, and REE contents but depleted in Sr, Zr, and Ti contents in comparison with worldwide examples of I-type granites (e.g., Almeida et al., 2007; Villaseca et al., 2009; Pérez-Soba and Villaseca, 2010), as well as the Gondwanan peraluminous I-type granites from Egypt (e.g., Abdel-Rahman and Martin, 1987; Figure 7b). It has the most resemblance with S-type granites (e.g., Antunes et al., 2008; Sheibi et al., 2012), as well as the Gondwanan peraluminous S-type granites from Tibet (e.g., Hu et al., 2015) (Figure 7b).

(5) Since S- and I-type granites derived from isotopically different sources, they have different $\delta^{18}O$ values. Oxygen isotope of quartz from granites provides a very effective discriminant for S- and I-type granites because quartz is less affected by alteration than whole rock (e.g. Harris et al., 1997). For example, quartz in I-type granites records

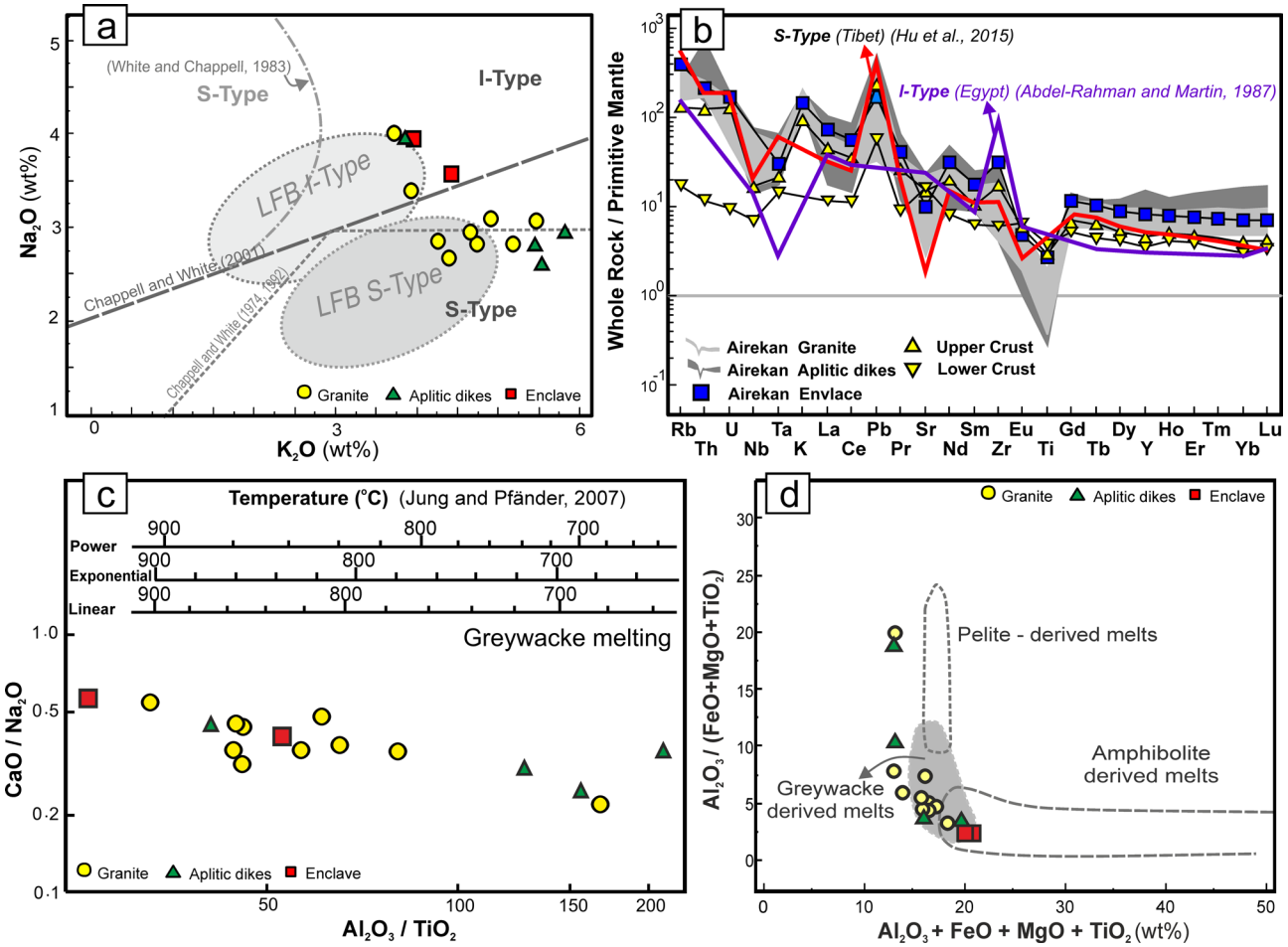

Figure 7. (a) Whole rock composition K_2O versus Na_2O diagram (field boundaries are after Chappell and White, 1974, 1992, 2001); (b) Primitive-normalized pattern for whole rock composition of granite and aplitic dike samples; (c) Al_2O_3/TiO_2 versus CaO/Na_2O diagram plotted by GCDKit 4.1 and thermometry based on psammite (~greywacke) melting (after Rapp and Watson, 1995; Jung and Pfänder, 2007); (d) Al_2O_3+FeO+MgO+TiO_2 versus Al_2O_3/(FeO+MgO+TiO_2) diagram (Patiño Douce, 1999).

$\delta^{18}O$ of approximately +6.6-11.8 ‰ (e.g., Bindeman and Valley, 2002; Öztürk et al., 2012; Lee et al., 2018; Kleine et al., 2018; Table S1). The quartz in S-type granites formed by partial melting of metapelitic rocks have $\delta^{18}O$ values between 11.2 to 14.0 ‰ (e.g., Harris and Vogeli, 2010; Lee et al., 2018). The Airekan pluton and crosscutting aplitic dikes contain quartz with average $\delta^{18}O$ values of 11.86 ‰ (n=8) and 12.28 (n=3), respectively (Table 5) and are comparable with the quartz in S-type granites formed by partial melting of metasedimentary rocks.

(6) The $\delta^{18}O$ values calculated for the Airekan granite magmas is 10.75 ‰, whereas it is 11.17‰ for the aplitic dikes (Table 5). According to Harris et al. (1997), these values (> 9.5 ‰) are similar to S-type granites.

Depth and P-T of crystallization

Airekan samples are comparable with the average composition of upper crust because they show enrichment in Rb, Th, U, Pb and Ta contents, but characteristically more depletion in Eu and Ti (Figure 7b), due to crystallization from a magma with segregation of plagioclase and ilmenite/sphene. In general, all S-type granites are apparently low-temperature in origin, however, the I-type granites with inherited zircons are also known as “low temperature” granites (e.g., Chappell et al., 2004). They are commonly associated with S-type granites and form by partial melting of quartzofeldspathic crust at low magmatic temperatures of ~700-800 °C (Chappell et al., 1998). Al_2O_3/TiO_2 ratio in the granitic magmas, which decreases with increasing temperature of crustal anatexis, indicates that fluid-absent melting of a psammite (~greywacke) source might have occurred at ~820 to 940 °C for the enclave, ~800 to 900 °C for granite, and ~650 to 720 °C for aplitic dikes (Figure 7c;

The wide range of Al_2O_3/TiO_2 values is probably related to later alterations). These temperatures, which are much higher than the water-saturated granite solidus, are in good agreement with an increase in the depth of crustal melting source from aplitic dikes toward granite, and enclaves.

Th+U and isotopic ratio of $^{206}Pb/^{238}U$ in the zircons (Table 4) correlate with decreasing of crystallization temperatures from their magmatic core to magmatic and then metamorphic overgrowths (Figure 6). For example, the magmatic events by Pan-African Orogeny from Cambrian (~518 Ma; Shirdashtzadeh et al., 2018) are recorded in the inherited cores with lower Th+U (Th+U ~444-895 ppm; $^{206}Pb/^{238}U>0.08$) (Figure 6b). Similar to findings by Smith et al. (2019), the inherited cores of zircons in Airekan granite resemble rounded detrital zircons by crustal reworking after crystallization from a pre-existing granitic source (Phase 1 in Figure 6a) with lower Th+U content (Figure 6b) and higher temperature in the deeper levels of crust. The Ordovician zircons (~483 Ma; Shirdashtzadeh et al., 2018) with magmatic nature are characterized with Th+U~590-2171 ppm and $^{206}Pb/^{238}U$~0.07-0.08 (Phase 2 in Figure 6b). These magmatic overgrowths could survived the inherited cores of Phase 1 in the granitic magma (Figure 6a), even at quite high temperatures (Clemens, 2003). Their Devonian (~382 Ma; Shirdashtzadeh et al., 2018) metamorphic darker rims (Phase 3 in Figure 6a) which were formed by Caledonian metamorphic events have Th+U of ~1002-3713 ppm and $^{206}Pb/^{238}U$ of <0.07 (Figure 6b). Thus, the outer dark rims indicate possible metamorphism that was obviously occurred at temperatures lower than the melting point of the host rock.

The zircons of phases 1 and 2 indicate that the primitive melts in Airekan area were saturated in Zr during melting. Following Watson and Harrison (1983) method, Zr saturation temperatures (685-853 °C) and Zr saturation levels (92.7-112.5 ppm) are calculated (Table 6) based on major elements and Zr concentrations (Table 3). The average Zr saturation temperatures of 740°C, 764 °C, and 853 °C are obtained for aplitic dikes, granite, and the enclave, respectively. Based on classification by Miller et al. (2003), granite and aplitic dike samples belong to the class of cold inheritance-rich granitoids with T_{Zr} <800 °C, while the enclaves are similar to hot inheritance-poor granitoids with T_{Zr} >800 °C. In addition to Zr saturation, the temperatures of phosphorus (apatite) saturation (averages: 823°C, 838°C, and 880 °C for aplitic dikes, granite, and the enclave, respectively) are calculated by following the method of Pichavant et al. (1992) (Table 6). In despite, T_{Zr} is not an accurate predictor of the onset of zircon crystallization in an initially zircon-undersaturated magma (Harrison et al., 2007), but as well as Al_2O_3/TiO_2 ratio, the calculated T_{Zr} and T_{Ap} can also confirm decreasing the depth of melts from enclave and granite

Table 6. Zircon and apatite saturation temperatures calculated based on major element and Zr compositions of Airekan aplitic dikes, granite, and enclave (north of Yazd Block, CEIM), using plugins in GCDkit 4.1 software (M=cationic ratios of 100(Na+K+2Ca)/(Al.Si); Zr=observed Zr concentrations; Zr_{sat}=saturation levels of Zr for assumed temperature; T_{Zr}=zircon saturation temperatures; T_{Ap}=apatite saturation temperature for peraluminous rocks).

Rock Type	Sample No.	M	Zr (ppm)	Zr_{sat} (ppm)	T_{Zr} (°C)	T_{Ap} (°C)
Granite	GR13	1.307501	210	96.6	817	813
	GR6	1.398620	137	104.4	773	850
	GR18	1.301025	47	96.1	695	836
	GR10	1.314271	174	97.2	800	846
	GR17	1.280929	149	94.5	788	828
	GR4	1.333648	146	98.8	783	868
	GR19	1.316293	123	97.4	769	837
	GR12	1.288130	52	95.1	703	789
	GR2	1.280728	118	94.5	768	866
	GR14	1.259028	83	92.7	741	852
Aplitic Dike	AD9	1.367890	309	101.7	849	822
	AD3	1.470532	47	111.0	685	-
	AD8	1.329334	66	98.4	719	843
	AD1	1.304263	56	96.4	708	805
Enclave	EN1	1.485929	355	112.5	852	880

to aplitic dikes.

Garnet is generally reported from both peraluminous and metaluminous granitoids (e.g., Patranabis-Deb et al., 2008; Samadi et al., 2014a), however, the absence of garnet from some peraluminous granites could be related to low MnO content of magma and/or pressures lower than lower crustal depths (~<5-7 kbar). MnO in the peraluminous S-type granite samples of Airekan (<0.05wt%; Table 3) is lower than the most of garnet-bearing granites (>0.1wt%) (e.g., the common whole rock compositions of garnet-bearing granites in: Wu et al., 2004; Samadi et al., 2014b; Rejash et al., 2018; etc.). Thus, the low MnO content of the primary melts hampered garnet formation. In fact, pressures in which mica dehydration has occurred were close to 10-15 kbars or even greater and then the rocks were mylonitized by uplifting along the local shear zones. The higher temperatures obtained for enclave samples could, therefore, be correlated with a hornblende-biotite dehydration melting process at ~800 to 920-970 °C/~10-15 kbar (Chen and Grapes, 2007), while the lower temperatures calculated for the granite and aplitic dikes are related to different degrees of biotite dehydration melting occurred at ~690-820 °C/~10-15 kbar (Chen and Grapes, 2007).

Protolith and magma genesis

The protolith composition, heat, pressure and water are essential requirements for crustal melting. Granitic magmas can be generated by partial melting of a wide variety of protolith materials and also as the end-products of extreme fractionation of mafic magmas (Clemens and Stevens, 2012). The S-type magmas are known to be a result of partial melting of metagreywackes (Clemens, 2003). Airekan samples are mostly similar to the melts derived from melting of greywackes (sandstones and metamorphosed quartzofeldspathic rocks), except for the melting source of enclave samples which seems to be metamorphosed igneous rocks (i.e., metagranites, amphibolite) (Figure 7d). The hydrous minerals dehydration (i.e. biotite, muscovite) in these crustal rocks, specially dehydration of biotite, is known to be the main anatectic melting mechanism giving rise to significant granite melt fractions at high thermal conditions (800 to 975 °C) at depth (e.g., Villaseca et al., 2009).

Granitic and aplitic rocks show similar whole rock composition (Figures 5d and 7b) and contain feldspar with similar trace and REE composition, suggesting no significant chemical changes during mylonitization. However, the aplite residues are known to be generated by extreme fractionation of the granitic magmas (e.g., Clemens and Stevens, 2012). In fact, according to studies of Finger and Schiller (2012), lower Ba/Pb ratios of aplitic dikes (~7; Table 3) are indicative of a lower-T anatectic event, while their host S-type granite with higher Ba/Pb ratios (~23; Table 3) shows a higher-T anatexis and larger partial melting.

After high degrees of partial melting of the crustal rocks, fractional crystallization of the voluminous anatectic magma resulted in decreasing normative components (i.e., Or, Ab, An, C, Hy, Ru, Ap, Il) as well as Al_2O_3, FeO, TiO_2, MgO, CaO, Na_2O, K_2O, P_2O_5, Ba, Rb, Ce, Eu, and V and ΣREE contents versus increase in silica content (Table 3) due to crystallization of different minerals. This fractionation is also traceable in rare and trace element patterns of feldspars. For example, whole rock normalized patterns of feldspar in the studied rocks (Figure 8), similarly indicate that REE and trace elements (e.g., Li, Rb, Y, Nb, Th, U, and Ta) contents of granitic magma were probably incorporated in formerly crystalized minerals (e.g., biotite and muscovite), while Sr, Pb, and Eu were mostly captured by plagioclase and then alkali-feldspar at the onset of feldspar fractionation from the melt. Sr fractionations were mainly controlled by feldspar crystallization rather than biotite based on the positive anomaly of Sr in feldspar/whole rock diagram (Figure 8). Low anorthite-content of plagioclases (i.e. albite) can be a consequence of evolving of magma in which the coefficient partitioning of plagioclase/melt increased and MgO/SiO_2 in the melt decreased (e.g., Bédard, 2006). Therefore, albite in the aplitic dikes which are crystallized from an evolved melt (with higher REE, Ga, Sc, Cu, Zn, Zr, Hf and Ti) has comparatively higher REE content.

The accessory minerals have a more crucial role in controlling the behavior of many elements (e.g., REE) in granitic systems rather than fractional crystallization of the main rock-forming minerals (e.g., Mittlefehldt and Miller, 1983). Saturation of zirconium and phosphorus in the primary fractionated silicate melts (e.g., Watson and Harrison, 1983) of Airekan has resulted in prior

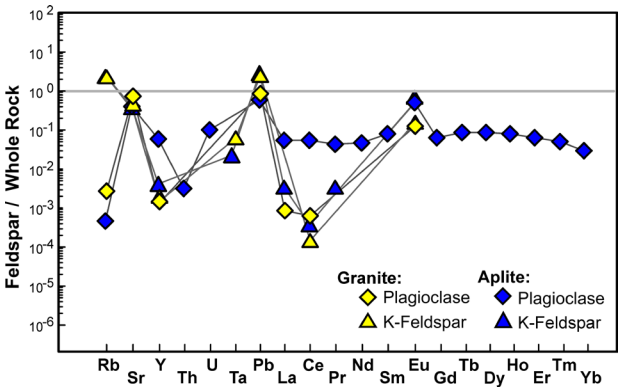

Figure 8. Whole rock-normalized pattern for feldspar composition in granite and aplitic dike of Airekan.

crystallization of zircon and apatite and consequently lowered REE and HREE/LREE contents in feldspar/whole rock pattern (Figure 8). Nevertheless, apatites have higher contents of LREE/HREE than zircons, so the apatite segregation could be more responsible for the weak decrease in LREE/HREE in feldspar (Figures 5a and 8). Anyway, the calculated zircon saturation temperatures (T_{Zr}) of 740 °C and 764 °C for aplitic dikes and granite are within the highest temperature range suggested for anatectic granitic/aplitic melts (~690-820 °C/~10-15 kbar; Chen and Grapes, 2007). By the way, the higher T_{Zr} for the enclave sample (853 °C) seems to be connected to an end-product melt of extreme fractionation of older melts.

Regional tectonomagmatic model

Magmatism

Continental collisional system is known as a common Ediacaran expression of Pan-African orogenic event (Liégeois, 1998). The Pan-African magmatism of the Iranian region can be thus tentatively interpreted as partial melting products of the crustal basement with minor mafic magma contribution (Rossetti et al., 2015) (Figures 9 a,b,b'). Granitic plutonism of Neoproterozoic -Cambrian is reported from several parts of the active continental margin of northern Gondwana, along the Alpine- Himalayan orogenic belt, from Europe, Menderes-Taurus block (southern Turkey), Northeast of Iran, CEIM, Pakistan, and India to the south of Tibet, during an orogenic system which is called Pan-African Orogeny (Kröner and Stern, 2004).

As it is concluded by Navidad et al. (2018, and references therein) for Eastern Pyrenees (southwest Europe), the northern Gondwana terranes recorded two magmatic stages: (1) first stage was occurred by waning activity of an active margin during the amalgamation of peri-Gondwana terranes at northern Gondwana at 620 and

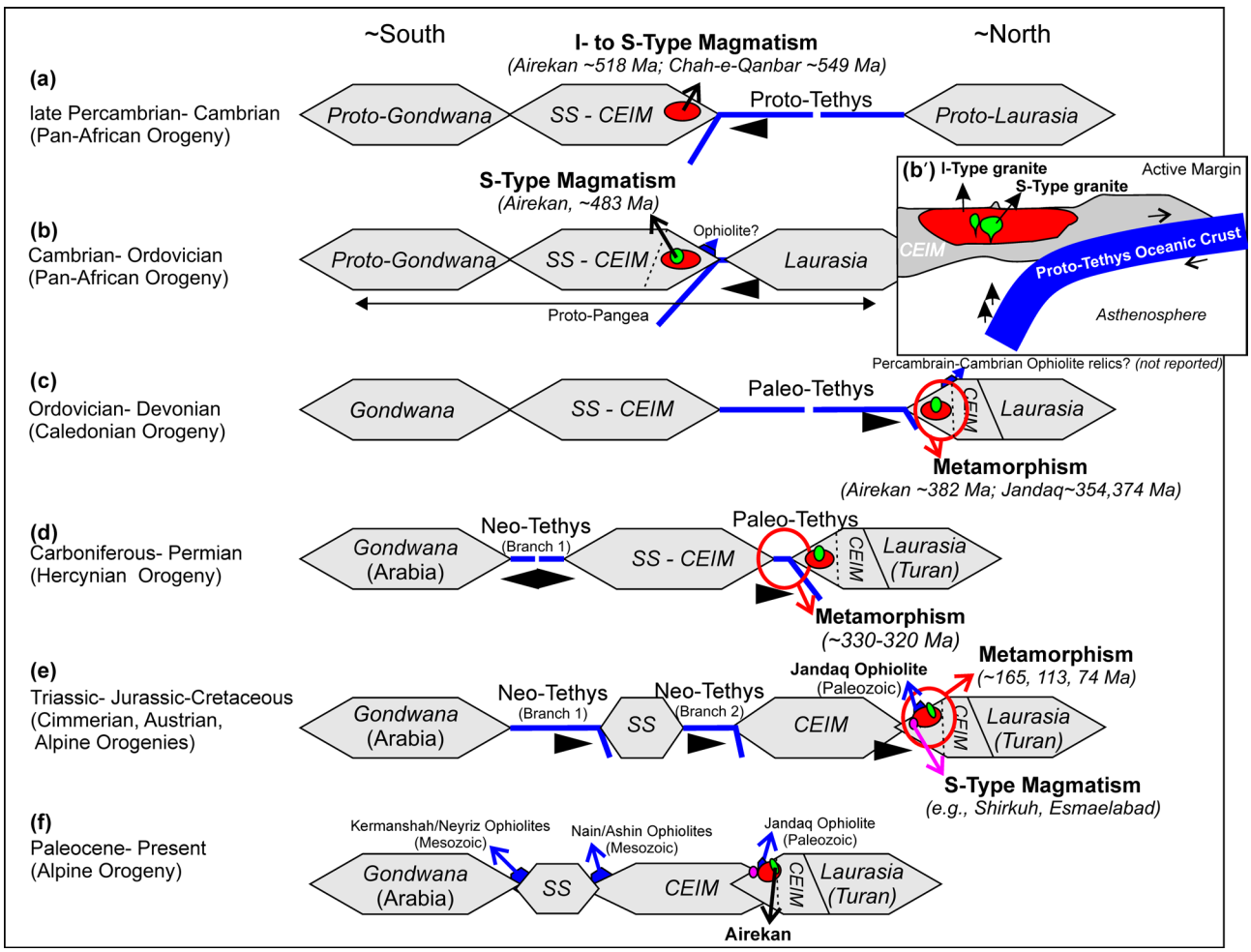

Figure 9. Schematic detailed pattern of structural, magmatic, and metamorphic events in CEIM from Precambrian to now (revised after Shirdashtzadeh et al., 2018), based on geochronological data by references in the text.

520 Ma; (2) second one was at Early-Middle Ordovician with peraluminous metagranites of crustal origin. These two stages are also detectable in the Middle East lands in: (1) Ediacaran-Early Cambrian, and (2) late Cambrian-early Ordovician. (Table 7). They are preserved in the continental fragments with Gondwanan affiliation, characterized by widespread late Neoproterozoic subduction-related magmatism (Table 7). For example, Ediacaran-Early Cambrian metaluminous-peraluminous subduction-related I-type granitic rocks in Turkey (e.g., Gursú et al., 2004; ~572 Ma in Ustaömer et al., 2012; ~550 Ma in Zlatkin et al., 2013), the late Pan-African calc-alkaline I-type granites in north-eastern Egypt in the north of Africa in the northern parts of Gondwana (~552 Ma; Abdel-Rahman and Martin, 1987), and the crystalline basement underlying the Sanandaj-Sirjan zone (e.g., Badr et al., 2018), Central Iran, and the Alborz Mountains (e.g., Hassanzadeh et al., 2008).

In the central parts of CEIM, the arc-related I- type granites in Zarigan (~525-527.9 Ma; Ramezani and Tucker, 2003), Chador-Malu (~529-525 Ma; Ramezani and Tucker, 2003), and S-type granites in Chah-e-Qanbar (~549 Ma; Bagheri and Stampfli, 2008), and also Airekan (~518.2 Ma for the inherited zircons of phase 1 in Airekan granite; Shirdashtzadeh et al., 2018) occurred during subduction of Ediacaran-Carboniferous Proto-Tethys ocean under the Gondwana terranes of CEIM in early Cambrian (Figure 9a). The enclaves with low-temperature I-type nature found in the Airekan pluton could be the preserved residues of a crystalline basement.

Then, magmatism was continued by Euramerica (Laurussia) and Gondwana continental collision (Figure

Table 7. Some examples of subduction-related felsic magmatism in the active margin of Proto-Tethys Ocean during Pan-African.

Magmatism Affinity	Granite Type	Region	Location	Example
Ediacaran–Early Cambrian:				
metaluminous-peraluminous subduction-related	I-type granitic rocks	north of Africa	north-eastern Egypt	~552 Ma (Abdel-Rahman and Martin, 1987)
		Turkey	Sandıklı area	(Gursú et al., 2004)
			Bitlis Massif	~572 Ma (Ustaömer et al., 2012)
			Menderes Massif	~550 Ma (Zlatkin et al., 2013)
		Sanandaj-Sirjan zone	Shahrekord Metamorphic Complex	(Badr et al., 2018)
		central parts of CEIM (Iran)	Zarigan	~525-527.9 Ma (Ramezani and Tucker, 2003)
			Chador-Malu	~529-525 Ma (Ramezani and Tucker, 2003)
	S-type granites	central parts of CEIM (Iran)	Chah-e-Qanbar	~549 Ma (Bagheri and Stampfli, 2008)
late Cambrian- early Ordovician:				
peraluminous subduction-related	S-type granites	northern Tibet	Qiangtang terrane	~486-480 Ma (Hu et al., 2015)
		CEIM (Iran)	Airekan	~483 Ma (Shirdashtzadeh et al., 2018)
		north-western Himalaya (Pakistan)	Mansehra Granitic Complex (MGC)	~478, 475 and 466 Ma (Naeem et al., 2016)

9b) and resulted in calc-alkaline magmatism in late Cambrian- early Ordovician. The Ordovician-Silurian high-K, calc-alkaline S-type granites from northern Tibet to south China (~486-480 Ma, Hu et al., 2015; 441-432 Ma, Wang et al., 2019), peraluminous S-Type Mansehra Granitic Complex (MGC) in the north-western Himalaya of Pakistan (~478, 475 and 466 Ma; Naeem et al., 2016), and early Ordovician high-K, calc-alkaline S-type granite of Airekan in the north of CEIM (~483 Ma for zircon of phase 2 in Shirdashtzadeh et al., 2018) are some of investigated examples for occurrence of this magmatism (Table 7). Based on the model of Bonin et al. (1998), this high-K calc-alkaline pluton may resemble a collisional stage in which a high-K calc-alkaline batholith derived from mantle sources and influenced by subducted crustal materials. However, the low content of Ta, Nb, and Ti (Figure 7b) is a crustal signature related to melting and anatexis of previously depleted metamorphosed igneous and/or pyroclastic sedimentary rocks in a subduction zone.

In the classification scheme by Barbarin (1999), the peraluminous S-type granite of Airekan is comparable with CCG (continental collisional granites) occurred in the region of continental collision between Gondwana (the west of CEIM in the northern margin of Gondwana) and Eurasia (the north of Yazd block) in late Cambrian to early Ordovician (Figure 9b). According to a model by Collins and Richards (2008), crustal melting in the arc and/or melting of a thickened crust in a possible backarc basin can be another feasible source to produce S-type granite (Figure 9b'). The other peraluminous S-type granites in the west of CEIM (i.e., Shirkuh and Esmael-Abad in the west of Yazd and Posht-e-Badam blocks) have formed later (i.e., Triassic to Jurassic), due to Triassic compression of CEIM by the Paleo-Tethys closure in its northeast and Neo-Tethys rifting in the west (Figure 9e).

Metamorphism and deformation

The high strain mylonitization features (e.g., GBM recrystallization in quartz, kinking and BLG in feldspars, foliation, etc.) indicate tectonic episodes during its emplacement in a shear zone at the depth of ~10 to 15 kilometers. In fact, continental collision between Euramerica (Laurussia) and Gondwana has led the north of Yazd block to undergo several metamorphic/deformation episodes (e.g., metamorphic complexes in Anarak, Jandaq and Posht-e-Badam). Some of them match the U-Pb age of 382.6 Ma for partial resetting of the U-Pb isotope system in the rims of zircons (zircon overgrowth of phase 3) from Airekan. For example, Bagheri and Stampfli (2008) suggested Ordovician to early Devonian for the metamorphism of metamorphic and ophiolitic complexes from Jandaq area to the south of Mohammad Abad (see Figure 1b) and Airekan. Berra et al. (2017) also have reported similar ages (~374, 354 Ma) from Jandaq area for the Paleo-Tethys evolution in the southern active margin of Laurasia. Then, Hercynian Orogeny in Carboniferous which resulted in spreading of Paleo-Tethys crust, its northward subduction (Figure 9c) and consequently, metamorphism at amphibolite facies in middle Carboniferous (~330-320 Ma, Ar-Ar dating; Bagheri and Stampfli, 2008) (Figure 9d).

Meanwhile, several left-lateral parallel faults with northeast- southwest trend (e.g., Great Kavir and Chupanan faults; Figure 1a) led exhumation and consequently cooling of granitic bodied (e.g., in Airekan, Mohammad Abad, and ChahQanbar; Figure 1b). This may be evidenced by closure temperatures and available metamorphic ages, from ~500 °C in Rb-Sr system of whole rock samples in ~165 Ma (Reyre and Mohafez, 1972), ~280 °C in K- Ar system of biotite in ~113 Ma (Reyre and Mohafez, 1972) and ~130 °C for alkali-feldspar in ~74 Ma (Reyre and Mohafez, 1972) (Figure 9e).

During Cimmerian orogeny, collision, northward subduction and accretion of several Gondwanan blocks (including Central Iran) to the southern margin of Eurasia occurred in Late Triassic and Early Jurassic, following the closure of the Paleo-Tethys Ocean (Zanchetta et al., 2013; Shafaii Moghadam et al., 2014 and references therein) (Figure 9e). In Upper Jurassic, the CEIM was located at low latitudes close to the Eurasian margin and it underwent significant counter-clockwise rotation during the Early Cretaceous (Mattei et al., 2015) during the orogenic activities of mid-Cimmerian, Austrian, and sub-Hercynian.

Finally, CEIM located between Arabia (Gondwana) and Turan plates (Laurasia) by the Cenozoic closure of Neo-Tethys and Alpine- Himalayan orogeny. The suture zones are defined by ophiolitic outcrops from Baft, Naein, Ashin and Jandaq (e.g., Shafaii Moghadam and Stern, 2014; Shirdashtzadeh et al., 2010, 2014; etc.).

CONCLUSIONS

The petrographical and geochemical characteristics of Airekan granite and associated aplitic dikes and enclaves elucidated the nature of a late Cambrian to early Ordovician magmatism related to Gondwana evolution during late Pan-African Orogeny in the north of CEIM. In the case of Airekan peraluminous pluton, the geochemical data (e.g., SiO_2>70 wt%, A/CNK>1, Rb>~160 ppm, Y <50 ppm, Th<30 ppm, Th/Ta>5, etc.) of the rocks as well as the $\delta^{18}O$ value of quartz crystals (average ~11.86‰; n=8) and presence of inherited zircons indicate an S-type granite with contribution of early Cambrian crustal materials melting during biotite and muscovite dehydration melting.

This peraluminous S-type intrusion has occurred in a collision-related system by crustal melting and fractional crystallization in the active continental margin of Gondwana as a consequence of Proto-Tethys Ocean closure in early Cambrian to early Ordovician in the north of CEIM. It shows geochronological and geochemical similarities with the other peraluminous granitic intrusions belonging to the Gondwana relics in the north of Africa, Turkey to Iran and Tibet. Thus, these northern Gondwana terranes recorded two magmatic stages: (1) first stage, including metaluminous-peraluminous I/S-type metagranites, generated during the amalgamation of peri-Gondwana terranes at Ediacaran-Early Cambrian; (2) second stage, including peraluminous S-type metagranites with crustal origin, began in late Cambrian-early Ordovician.

ACKNOWLEDGEMENTS

This project was sponsored by the Iranian National Science Foundation (INSF) and University of Isfahan under grant number 94028981. The authors acknowledge the Kanazawa University (Kanazawa, Japan), the NRF (South Africa) and Professor Bruce Schafer at Macquarie GeoAnalytical (MQGA) in Macquarie University (Australia) for financial support, providing geochemical facilities, and the scientific and technical assistance. Authors appreciate all the constructive comments and suggestions from Dr. Alessandro Fabbrizio and anonymous journal reviewer, which helped us to improve the quality of the article.

REFERENCES

Abdel-Rahman A.M. and Martin R.F., 1987. Late Pan-African magmatism and crustal development in northeastern Egypt. Geological Journal 22, 281-301.

Abdel-Rahman A.M., 1994. Nature of biotites from alkaline, calc-alkaline, and peraluminous Magmas. Journal of Petrology 35, 525-54.

Alavi M., 1991. Sedimentary and structural characteristics of the Paleo-Tethys remnants in northeastern Iran. Geological Society of America Bulletin 103, 983-992.

Almeida M.E., Macambira M.J.B., Oliveira E.C., 2007. Geochemistry and zircon geochronology of the I-type high-K calc-alkaline and S-type granitoid rocks from southeastern Roraima, Brazil: Orosirian collisional magmatism evidence (1.97-1.96 Ga) in central portion of Guyana Shield. Precambrian Research 155, 69-97.

Antunes I.M.H.R., Neiva A.M.R, Silva M.M.V.G., Corfu F., 2008. Geochemistry of S-type granitic rocks from the reversely zoned Castelo Branco pluton (central Portugal). Lithos 103, 445-465.

Badr A., Davoudian A.R., Shabanian N., Azizi H., Asahara Y., Neubauer F., Dong Y., Yamamoto K., 2018. A- and I-type metagranites from the North Shahrekord Metamorphic Complex, Iran: Evidence for Early Paleozoic post-collisional magmatism. Lithos 300-301, 86-104.

Bagheri S. and Stampfli G.M., 2008. The Anarak, Jandaq and Posht-e-Badam metamorphic complex in central Iran: New geological data, relationships and tectonic implications. Tectonophysics 451, 123-155.

Barbarin B., 1999. A review of the relationships between granitoid types, their origins and their geodynamic environments. Lithos 46, 605-626.

Bédard J.H., 2006. Trace element partitioning in plagioclase feldspar. Geochimica et Cosmochimica Acta 7, 3717-3742.

Bell E.A., Boehnke P., Harrison T.M., 2017. Applications of biotite inclusion composition to zircon provenance determination. Earth and Planetary Science Letters 473, 237-246.

Berra F., Zanchi A., Angiolini L., Vachard D., Vezzoli G., Zanchetta S., Bergomi M., Javadi H.R., Kouhpeyma M., 2017. The upper palaeozoic Godar-e-Siah Complex of Jandaq: Evidence and significance of a north Palaeotethyan succession in Central Iran. Journal of Asian Earth Sciences 138, 272-290.

Bindeman I.N. and Valley J.W., 2002. Oxygen isotope study of the Long Valley magma system, California: isotope thermometry and convection in large silicic magma bodies. Contributions to Mineralogy and Petrology 144, 185-205.

Bokhari S.N.H. and Meisel T.C., 2017. Method Development and Optimisation of Sodium Peroxide Sintering for Geological Samples. Geostandards and Geoanalytical Research 41, 181-195.

Bonin B., Azzouni-Sekkal A., Bussy F., Ferrag S., 1998. Alkali-calcic and alkaline post-orogenic (PO) granite magmatism: petrologic constraints and geodynamic settings. Lithos 45, 45-70.

Chappell B.W. and White A.J.R., 1974. Two contrasting granite types. Pac Geology 8, 173-174.

Chappell B.W. and White A.J.R., 2001. Two contrasting granite types - 25 years later. Australian Journal of Earth Sciences 48, 489-499.

Chappell B.W., 1999. Aluminum saturation in I- and S-type granites and the characterization of fractional haplogranites. Lithos 46, 535-551.

Chappell B.W., White A.J.R., Williams I.S., Wyborn D., 2004. Low- and high-temperature granites. Transactions of the Royal Society of Edinburgh: Earth Sciences 95, 125-140.

Chen G. and Grapes R., 2007. Granite Genesis: In Situ Melting and Crustal Evolution. Springer, Netherlands.

Clemens J.D. and Stevens G., 2012. What Controls Chemical Variation in Granitic Magmas? Lithos 134-135, 317-329.

Clemens J.D., 2003. S-type granitic magmas-petrogenetic issues, models and evidence. Earth-Sciences Review 61, 1-18.

Collins W.J. and Richards S.W., 2008. Geodynamic significance of S-type granites in circum-Pacific orogens. Geology 36,

559-562.

Deer W.A., Howie R.A., Zussman J., 2013. An introduction to the rock forming minerals. 3rd excerpted student edition. Geological Society of London/UK, 505 pp.

Didier J. and Barbarin B., 1991. Enclaves Enclaves and Granite Petrology. Developments in Petrology 13, Elsevier Amsterdam, 625 pp.

Finger F. and Schiller D., 2012. Lead contents of S-type granites and their petrogenetic significance. Contributions to Mineralogy and Petrology 164, 747-755.

Fourie D.S. and Harris C., 2011. O-isotope study of the Bushveld Complex granites and granophyres: Constraints on Source composition, and assimilation. Journal of Petrology 52, 2221-2242.

Frost B.R., Barnes C.G., Collins W.J., Arculus S.R.J., Ellis D.J., Frost C.D., 2001. A geochemical classification for granitic rocks. Journal of Petrology 42, 2033-2048.

Gursú S., Göncüoglu M.C., Bayhan H., 2004. Geology and Geochemistry of the Pre-early Cambrian Rocks in the Sandikli Area: Implications for the Pan-African Evolution of NW Gondwana. Gondwana Research 7, 923-935.

Harris C. and Vogeli J., 2010. Oxygen isotope composition of garnet in the Peninsula Granite, Cape Granite Suite, South Africa: Constraints on melting and emplacement mechanisms. South African Journal of Geology 13, 401-412.

Harris C., Faure K., Diamond R.E., Scheepers R., 1997. Oxygen and hydrogen isotope geochemistry of S- and I-type granitoids: The Cape Granite suite, South Africa. Chemical Geology 143, 95-114.

Harrison T.M., Watson E.B., Aikman A.B., 2007. Temperature spectra of zircon crystallization in plutonic rocks. Geology 35, 635-638.

Hassanzadeh J., Stockli D.F., Horton B.K., Axen, G.J., Stockli, L.D., Grove M., Schmitt A.K., Walker J.D., 2008. U-Pb zircon geochronology of late Neoproterozoic- Early Cambrian granitoids in Iran: Implications for paleogeography, magmatism, and exhumation history of Iranian basement. Tectonophysics 451, 71-96.

Hu P.Y., Zhai Q., Jahn B., Tang S., 2015. Early Ordovician granites from the South Qiangtang terrane, northern Tibet: Implications for the early Paleozoic tectonic evolution along the Gondwanan proto-Tethyan margin. Lithos 220-223, 318-338.

Jung S. and Pfänder J.A., 2007. Source composition and melting temperatures of orogenic granitoids: constraints from CaO/Na_2O, Al_2O_3/TiO_2 and accessory mineral saturation thermometry. European Journal of Mineralogy 19, 859-870.

Kleine B.I., Stefánsson A., Halldórsson S.A., Whitehouse M.J., Jónasson K., 2018. Silicon and oxygen isotopes unravel quartz formation processes in the Icelandic crust. Geochemical Perspectives Letters 7, 5-11.

Kröner A. and Stern R.J., 2004. Pan-African Orogeny. Encyclopaedia of Geology. Elsevier, Amsterdam 1, 1-12.

Lee S.G., Ahn I., Asahara Y., Tanaka T., Lee S.R., 2018. Geochemical interpretation of magnesium and oxygen isotope systematics in granites with the REE tetrad effect. Geosciences Journal 22, 697-710.

Li S., Zhao S., Liu X., Cao H., Yu S., Li X., Somervillec I., Yu S., Suo Y., 2017. Closure of the Proto-Tethys Ocean and Early Paleozoic amalgamation of microcontinental blocks in East Asia. Earth-Science Review 186, 37-75.

Liégeois J-P., Navez J., Hertogen J., Black R., 1998. Contrasting origin of post-collisional high-K calc-alkaline and shoshonitic versus alkaline and peralkaline granitoids. The use of sliding normalization. Lithos 45, 1-28.

Liu X., Li X., Liu Y., Yang L., Li Q., Wu F., Yu H., Huang F., 2018. Insights into the origin of purely sediment-derived Himalayan leucogranites: Si-O isotopic constraints. Science Bulletin 63, 1243-1245.

McDonough W.F. and Sun S.S., 1995. The composition of the Earth. Chemical Geology 120, 223-253.

Meert J.G. and Van Der Voo R., 1997. The assembly of Gondwana 800-550 Ma. Journal of Geodynamics 23, 223-235.

Meisel T.C., Schöner N., Paliulionyte V., Kahr E., 2002. Determination of rare earth elements, Y, Th, Zr, Hf, Nb and Ta in geological reference materials G-2, G-3, SCo-1 and WGB-1 by sodium peroxide sintering and Inductively Coupled Plasma-Mass Spectrometry. Geostandards Newsletter, Geostandards and Geoanalytical Research 26, 53-61.

Miller C.F., McDowell S.M., Mapes R.W., 2003. Hot and cold granites? Implications of zircon saturation temperatures and preservation of inheritance. Geology 31, 529-532.

Mittlefehldt D.W. and Miller C.F., 1983. Geochemistry of Sweetwater Wash pluton, California: implications for 'anomalous' trace element behavior during differentiation of felsic magmas. Geochimica et Cosmochimica Acta 47, 109-124.

Mosavi Makoi A., 1998. Petrology of Narigan Granite, M.Sc. thesis, Shahid Beheshti University, Tehran, Iran. Published thesis (in Persian).

Muttoni G., Mattei M., Balini M., Zanchi A., Gaetani M., Berra F., 2009. The drift history of Iran from the Ordovician to the Triassic, In; Brunet, MF, Wilmsen, M, Granath, JW (Eds.), South Caspian to Central Iran Basins. Geological Society, London, Special Publications 312, 7-29.

Nadimi A., 2007. Evolution of the central Iranian basement. Gondwana Research 12, 324-333.

Naeem M., Burg J.P., Ahmad N., Chaudhry M.N., Khalid P., 2016. U-Pb zircon systematics of the Mansehra Granitic Complex: implications on the early Paleozoic orogenesis in NW Himalaya of Pakistan. Geoscience Journal 20, 427-447.

Navidad M., Castiñeiras P., Casas J.M., Liesa M., Belousova E., Proenza J., Aiglsperger T., 2018. Ordovician magmatism in the eastern Pyrenees: Implications for the geodynamic evolution of northern Gondwana. Lithos 314-315, 479-496.

O'Connor J.T., 1965. A classification of quartz-rich igneous rock based on feldspar ratios. US Geological Sur, Prof Paper 525B, B79-B84.

Öztürk Y.Y., Helvaci C., Satir M., 2012. Geochemical and isotopic constraints on petrogenesis of the Beypazarı Granitoid, NW Ankara, Western Central Anatolia, Turkey. Turkish Journal of Earth Science 21, 53-77.

Papike J.J., 1988. Chemistry of the rock-forming silicates: Multiple-chain, sheet, and framework structures. Reviews of Geophysics 26, 407-444.

Passchier C.W. and Trouw R.A.J., 2005. Microtectonics. Springer-Verlag, New York.

Patiño Douce A.E., 1999. What do experiments tell us about the relative contributions of crust and mantle to the origins of granitic magmas? In: Understanding granites: integrating new and classical techniques. (Eds.): Castro A., Fernandez C., Vigneresse J.L., Geological Society of London, Special Publication 168, 55-75.

Patranabis-Deb A., Schieber J., Basu A., 2008. Almandine garnet phenocrysts in a ~1Ga rhyolitic tuff from Central India. Geological Magazine, 1-11.

Pérez-Soba C. and Villaseca C., 2010. Petrogenesis of highly fractionated I-type peraluminous granites. La Pedriza pluton (Spanish Central System). Geologica Acta 8, 131-149.

Pichavant M., Montel J-M., Richard L.R., 1992. Apatite solubility in peraluminous liquids: Experimental data and an extension of the Harrison model. Geochimica et Cosmochimica Acta 56, 3855-3861.

Ramezani J. and Tucker R.D., 2003. The Saghand region, central Iran: U-Pb geochronology, petrogenesis and implications for Gondwana tectonics. American Journal of Science 303, 622-665.

Rapp R.P. and Watson E.B., 1995. Dehydration melting of metabasalt at 8-32 kbar: implications for continental growth and crust-mantle recycling. Journal of Petrology 36, 891-931.

Reyre D. and Mohafez S., 1972. A first Contribution of the NIOC-ERAP Agreements to the Knowledge of Iranian Geology. Edition Technip Paris, 1-58.

Romanko E., Susov M., Dvoryankin A., Selivanov Tkachev E-G., Krivyakin B., Morozov L., Silaev V., Kiristaev V., Desyaterik N., 1979. Geology and minerals of Jandaq area (Central Iran). Technoexport Report, TE/NO. 4

Rossetti F., Nozaem R., Lucci F., Vignaroli G., Gerdes A., Nasrabadi M., Theye T., 2015. Tectonic setting and geochronology of the Cadomian (Ediacaran-Cambrian) magmatism in Central Iran, Kuh-e-Sarhangi region (NW Lut Block). Journal of Asian Earth Sciences 102, 24-44.

Samadi R., Gazel E., Mirnejad H., Kawabata H., Baharifar A.A., Sheikh-Zakaraiee S.J., 2014b. Paleo-Tethys subduction in the center of the Alpine-Himalayan orogenic system in the Triassic: Evidence from geochemistry of I-type granitoids from Dehnow pluton, NE Iran. Neues Jahrbuch für Geologie und Paläontologie, Abhandlungen 271, 285-306.

Samadi R., Mirnejad H., Kawabata H., Valizadeh M.V., Harris C., Gazel E., 2014a. Magmatic garnet in the Triassic (215 Ma) Dehnow pluton of NE Iran and its petrogenetic significance. International Geology Review 56, 596-621.

Shafaii Moghadam H. and Stern R.J., 2014. Ophiolites of Iran: Keys to understanding the tectonic evolution of SW Asia: (I) Palaeozoic ophiolites. Journal of Asian Earth Sciences 91, 19-38.

Shafaii Moghadam H., Li X-H., Stern R.J., Santos J.F., Ghorbani G., Pourmohsen M., 2016. Age and nature of 560-520 Ma calc-alkaline granitoids of Biarjmand, northeast Iran: insights into Cadomian arc magmatism in northern Gondwana. International Geology Review 58, 1492-1509.

Sheibi M., Bouchez J.L., Esmaeily D., Siqueira R., 2012. The Shir-Kuh pluton (Central Iran): Magnetic fabric evidences for the coalescence of magma batches during emplacement. Journal of Asian Earth Sciences 46, 39-51.

Shirdashtzadeh N., 2017. Petrology and geochemistry of S-type granitoid intrusion of the Airekan area (North of Khur, Central Iran) and its role in the formation of radioactive deposit of Cheshmeh-Shotori. Final Post-Doctoral Report, Department of Geology, University of Isfahan, Isfahan, Iran. Published report (with English Abstract).

Shirdashtzadeh N., Torabi G., Arai S., 2010. Metamorphism and metasomatism in the Jurassic Nain ophiolitic mélange, Central Iran. Neues Jahrbuch für Geologie und Paläontologie, Abhandlungen 255, 255-275.

Shirdashtzadeh N., Torabi G., Meisel T.C., Arai S., Bokhari S.N.H., Samadi R., Gazel E., 2014. Origin and evolution of metamorphosed mantle peridotites of Darreh Deh (Nain Ophiolite, Central Iran): Implications for the Eastern Neo-Tethys evolution. Neues Jahrbuch für Geologie und Paläontologie, Abhandlungen 273, 89-120.

Shirdashtzadeh N., Torabi G., Schaefer B., 2018. A magmatic record of Neoproterozoic to Paleozoic convergence between Gondwana and Laurasia in the northwest margin of the Central-East Iranian Microcontinent. Journal of Asian Earth Sciences 166, 35-47.

Smith W.D., Darling J.R., Bullen D.S., Lasalle S., Pereira I., Moreira H., Allen C.J., Tapster S., 2019. Zircon perspectives on the age and origin of evolved S-type granites from the Cornubian Batholith, Southwest England. Lithos 336-337, 14-26.

Susov M., Dvoryankin A., Selivanov V., Maksimova I., 1984. Gological map of Arusan. scale 1: 100000, sheet 705, USSR Ministry of Geology, V/O Technoexport.

Taylor S.R. and McLennan S.M., 1981. The composition and evolution of the continental crust: rare earth element evidence from sedimentary rocks. Philosophical Transactions of the Royal Society 301, 381-399.

Ustaömer P.A., Ustaömer T., Gerdes A., Collins A.S., 2012. Evidence of Precambrian sedimentation/ magmatism and Cambrian metamorphism in the Bitlis Massif, SE Turkey

utilising whole-rock geochemistry and U-Pb LA-ICP-MS zircon dating. Gondwana Research 21, 1001-1018.

Verdel C., Wernicke B.P., Renne P.R., Spell T.L., 2007. Geology and thermochronology of Tertiary Cordilleran-style metamorphic core complexes in the Saghand region of Central Iran. Geological Society of America Bulletin 119, 961-977.

Villaseca C., Bellido F., Pérez-Soba C., Billström K., 2009. Multiple crustal sources for post-tectonic I-type granites in the Hercynian Iberian Belt. Mineralogy and Petrology 96, 197-211.

von Raumer J. and Stampfli G.M., 2008. The birth of the Rheic Ocean - Early Palaeozoic subsidence patterns and tectonic plate scenarios. Tectonophysics 461, 9-20.

Wang Y., Li G., Wang Q., Santosh M., Chen J., 2019. Early Paleozoic granitoids from South China: implications for understanding the Wuyi-Yunkai orogeny. International Geology Review 62, 243-261.

Watson E. and Harrison T., 1983. Zircon saturation revisited: temperature and compositional effects in a variety of crustal magma types. Earth and Planetary Science Letters 64, 295-304.

Whitney D.L. and Evans B.W., 2010. Abbreviations for names of rock-forming minerals. American Mineralogist 95, 185-187.

Wu F., Sun D., Jahn B., Wilde S., 2004. A Jurassic garnet-bearing granitic pluton from NE China showing tetrad REE patterns. Journal of Asian Earth Sciences 23, 731-744.

Zlatkin O., Avigad D., Gerdes A., 2013. Evolution and provenance of Neoproterozoic basement and Lower Paleozoic siliciclastic cover of the Menderes Massif (western Taurides): Coupled U- Pb- Hf zircon isotope geochemistry. Gondwana Research 23, 682-700.